




Seismotectonic aspects of the M_s 7.3 1948 October 5 Aşgabat (Ashgabat) earthquake, Türkmenistan: right-lateral rupture across multiple fault segments, and continuing urban hazard

N. Marshall ¹, Q. Ou,^{1,2} G. Begenjev,³ E. Bergman,⁴ Y. Bezmenov,³ N. Dodds ¹, C. Gruetzner,⁵ T. Hudson,¹ I. Pierce,¹ R. Mirzin,³ E. Rhodes,^{6,7} R.T. Walker ¹ and P. Wordsworth⁸

¹COMET, Department of Earth Sciences, Oxford University, Oxford OX1 3AN, UK. E-mail: neill.marshall@earth.ox.ac.uk

²COMET, University of Leeds, Leeds LS2 9JT, UK

³Institute of Seismology and Physics of the Atmosphere, National Academy of Sciences of Türkmenistan, Aşgabat 744000, Türkmenistan

⁴Global Seismological Services, 190019th St., Golden, CO 80401, USA

⁵Friedrich Schiller University Jena, Institute of Geological Sciences, Jena 07749, Germany

⁶Department of Geography, University of Sheffield, Sheffield S102TN, UK

⁷Department of Earth, Planetary, and Space Sciences, University of California Los Angeles, Los Angeles, CA 90095-1567, USA

⁸School of Archaeology, University of Oxford, Oxford OX1 3TG, UK

Accepted 2023 December 20. Received 2023 November 21; in original form 2023 June 1

SUMMARY

The M_s 7.3 1948 Aşgabat earthquake was one of the most devastating earthquakes of the 20th century, yet little is known about its location, style and causative fault. In this study, we bring together new seismic and geomorphic observations with previously published descriptions of surface rupture and damage distributions to determine the likely source of the earthquake. We determine the epicentre and focal mechanism of this earthquake from digitized historical seismograms and the relocation of regional seismicity to show that the earthquake most likely nucleated close to the city of Aşgabat. The earthquake ruptured a right-lateral strike-slip fault to the southeast of the city, which has a clear long-term expression in the landscape, and also likely reactivated a subparallel concealed thrust along the Gyaursdag anticline east of the city. The earthquake potentially also ruptured a right-lateral segment northwest of Aşgabat, which does not have an identifiable expression in the landscape. Using high-resolution satellite imagery and digital elevation models we investigate the geomorphology of active faulting around Aşgabat and adjacent parts of the Köpetdag (Kopeh Dag) mountain range front, showing that there are significant strike-slip and oblique strike-slip segments adjacent to the city that apparently did not rupture in 1948, and yet show clear geomorphic expression and potential right-lateral displacement of Parthian-era (~ 2000 yr) and post-Sassanian era (~ 1500 yr) archaeological remains. Luminescence dating of displaced fluvial terraces west of Aşgabat yields a vertical displacement rate of 0.6 mm yr^{-1} , though the strike-slip rate remains undetermined.

Key words: Asia; Earthquake hazards; Earthquake source observations; Seismicity and tectonics; Continental neotectonics; Continental tectonics: strike-slip and transform.

1 INTRODUCTION

At 01:12 a.m. local time on 5 October 1948 a M_w 7.3 earthquake occurred near the city of Aşgabat in present-day Türkmenistan (Orasymbetov *et al.* 1960; Sidorin 2019). The city was almost destroyed, and its population devastated by the main shock and subsequent aftershocks. It is estimated that 90 per cent of all buildings in the city collapsed killing between 68 000 and 120 000 people

(Nikonov 1998; Sidorin 2019) making this one of the most damaging earthquakes recorded in the 20th century (England & Jackson 2011). Despite the size and impact of this earthquake, there are continuing uncertainties in the location, mechanism and causative fault. There is disagreement about the mechanism of this earthquake, which range between strike-slip and thrust mechanisms (Rezanov 1957; Shirokova 1967; Mckenzie 1972; Tchalenko 1975; Nikonov 1998; Berberian & Yeats 2001; Sidorin 2019). A wide array of

surface ruptures has been reported in earlier publications (e.g. Rogozhin 1995; Sidorin 2019), though significant urban expansion and regional development during the last 30 yr may have masked any residual surface signals that could have been preserved. Furthermore, the active faulting around Aşgabat and surrounding areas has not been mapped in detail, such that the tectonic context of the 1948 earthquake is not clear.

Determining the location, magnitude, focal mechanism and rupture style of large earthquakes that occur in this region is of vital importance for understanding local seismic hazard, and for improving our broader understanding of the regional tectonics and large-scale fault systems that accommodate shortening (e.g. Walker *et al.* 2021). The potential for stepover during the Aşgabat rupture may allow this earthquake to help us understand the processes that control multifault and multisegment ruptures, which have been shown to be important through several strike-slip occurrences in recent years [e.g. the M 7.8 and 7.5 2023 Kahramanmaraş (Barbot *et al.* 2023) and the M 7.1 2019 Ridgecrest (Antoine *et al.* 2021) earthquakes].

In this paper, we investigate the source of the 1948 Aşgabat earthquake. We combine seismic investigations, intensity distributions, contemporary mapping of surface rupture and analysis of high-resolution optical satellite data and derived topographic data sets and field-based quaternary dating. Our seismic investigations of the earthquake source parameters are aided by digitized analogue seismograms sourced from a range of global archives and through compilation of bulletin arrival times. Epicentral location and depths of earthquakes in Turkmenistan are determined using a calibrated multiple event relocation technique (Bergman *et al.* 2022).

2 BACKGROUND AND REGIONAL SETTING

2.1 Tectonics

Aşgabat (Ashgabat) [population 864 000 (<https://data.worldbank.org/>)] is the capital city of Turkmenistan (Turkmenistan) and sits at the northernmost edge of the Eurasia–Arabia continental collision (Fig. 1). Deformation in Turkmenistan results from a combination of north–south shortening associated with the Eurasia–Arabia collision, and by the motion of the South Caspian Basin (SCB). The South Caspian Basin is an aseismic block moving independently of its surroundings, with a rate of $10 \pm 2 \text{ mm yr}^{-1}$ in direction $330^\circ \pm 10^\circ$ relative to Eurasia (Jackson *et al.* 2002; Copley & Jackson 2006; Djamour *et al.* 2010; Walker *et al.* 2021; Dodds *et al.* 2022a). The South Caspian's motion relative to its surroundings is accommodated along left-lateral strike-slip faults of the Alborz mountains in Iran, and along the oblique right-lateral reverse Main Köpetdag fault (MKDF) in Turkmenistan, which has a geological slip-rate at $9.1 \pm 1.3 \text{ mm yr}^{-1}$ (Walker *et al.* 2021) and InSAR-derived geodetic right-lateral slip-rate $9 \pm 2 \text{ mm yr}^{-1}$, and a shortening rate of $4 \pm 2 \text{ mm yr}^{-1}$ (Dodds *et al.* 2022b).

The tectonics of the Köpetdag range change along strike, from rapid right-lateral faulting related to South Caspian Basin–Eurasia in the west, through to north–south Arabia–Eurasia shortening in the east. The transition between these two domains likely occurs within the Barharden–Quchan fault zone (BQFZ; Fig. 1), centred on longitude $\sim 58^\circ\text{E}$, which consists of an array of NNW–SSE trending right-lateral faults that cut through the Köpetdag range (Hollingsworth *et al.* 2006, 2008; Shabanian *et al.* 2009). Aşgabat, where the destructive 1948 earthquake occurred, lies near the eastern margin of the BQFZ.

2.2 Earthquakes

The 1948 earthquake is the most destructive event in Turkmenistan, though not the only significant event in recent history (Ambraseys 1997; Berberian & Yeats 2001; Dodds *et al.* 2022a). Significant earthquakes in 1895, 1946, 1983, 1984 and 2000 have occurred in the eastern Caspian lowlands (Fig. 2, also see Section 4.3). The 1983 and 1984 events were associated with surface rupture near Kumdag town (Fig. 2a), indicative of right-lateral faulting on a NW–SE trend (e.g. Jackson *et al.* 2002). Closer to Aşgabat there have been several large earthquakes on the right-lateral faults of the BQFZ, within the interior of the Köpetdag. These include the 1851, 1871, 1872, 1893 and 1895 Quchan earthquake sequence with $M \sim 6.8\text{--}7.2$, the May 1st 1929 ($M_s \sim 7$) Baghan earthquake, which produced up to 50 km of surface rupture (Tchalenko 1975) and the 4 February 1997 Bojnurd earthquake with M_w 6.4 (Hollingsworth *et al.* 2006).

Instrumentally recorded earthquakes in the eastern part of Turkmenistan and adjacent parts of Iran, east of longitude 55°E , have centroid depths typically less than 20 km, whereas those west of 55°E are deeper, with centroid depths ranging between 20 and 50 km (Jackson *et al.* 2002; Walker *et al.* 2021). The deeper earthquakes west of 55°E are likely to reflect increasing thickness of sediment in the east Caspian lowlands, and the influence of the South Caspian basement. Available focal mechanisms show strike-slip faulting (right-lateral on NW–SE planes, or left-lateral on NE–SW planes) as far east as 60°E .

There are relatively few recorded earthquakes along the Köpetdag range front between Aşgabat and Bereket. Dodds *et al.* (2022a) observed a single palaeo-earthquake rupture with average offsets of $\sim 7.5 \text{ m}$ along a $\sim 200\text{-km}$ -long section of the MKDF from Bereket to Arçman. They estimate a magnitude of M_w 7.8 and an age of 600–800 yr based on trenching and the displacement of cultural features of presumed Medieval age. East of Arçman to Aşgabat the Köpetdag range front is more segmented, and is separated into the Baharly, Dowgala and Goktepe segments. The only constraint on earthquake timing along this part of the range front is provided by two infrared-stimulated luminescence (IRSL) ages of 3.4 ± 0.5 26 ka and 2.5 ± 0.2 ka from a river cutting exposure of an alluvial fan surface along the Baharly segment predating the most-recent surface rupture.

Berberian & Yeats (2001) report archaeological evidence for destructive earthquakes in proximity to Aşgabat, with inferred earthquake damage at the Parthian city of Old Nisa dated from the first century 179 BCE to the first century CE (Pilipko 2007) and from the Bronze Age settlement of Ak-Depe at 3000–2000 BCE (Liapin 2006). However, as noted by Dodds *et al.* (2022a,b), both the interpretation of the damage and the dating are ambiguous, and other potential dates of earthquake damage are possible. For instance, a date of the fifth century CE is proposed by earlier excavators at Nisa, but does not appear in later publications (Davidovich 1951).

3 METHODS

3.1 Remote sensing

We mapped active faults using a combination of modern imagery of different resolutions and digitized historical fault, rupture and intensity maps recorded by Soviet scientists after the 1948 earthquake (Rogozhin 1995; Sidorin 2019). The Soviet records have been georeferenced using the QGIS 3.16 software (QGIS Development Team 2021), though challenges in accurately georeferencing the maps to modern imagery means they should be used as a guide only. We

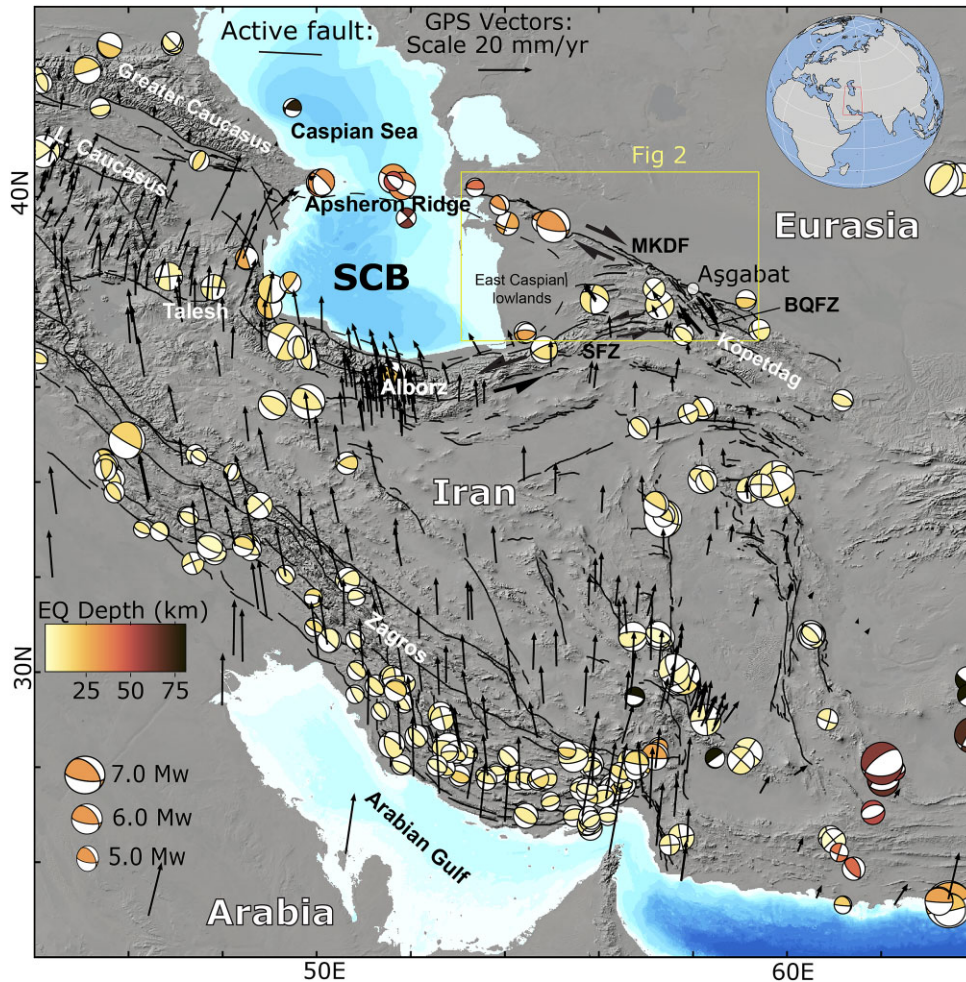


Figure 1. Tectonic map of the Arabian–Eurasian Plate collision zone. Black arrows represent GPS velocity vectors after Khorrani *et al.* (2019) relative to Eurasia. Waveform-modelled focal mechanism solutions and locations for earthquakes greater than M_w 3.5 between 1917 and 2017 from the catalogue created by Wimpenny & Watson (2020); blue lines show active faults in the region (Walker *et al.* 2021). Digital Elevation Model (DEM) from SRTM 90 m (NASA 2013). Main Köpetdag Fault zone—MKDF; South Caspian Basin—SCB (black dotted line); Baherden–Quchan Fault Zone—BQFZ and Shahrud Fault Zone—SFZ.

traced from these maps the reported and recorded ruptures shown in Fig. 3.

To analyse the geomorphological signature of earthquake ruptures and fault scarps we used tri-stereo high-resolution Pléiades imagery and bi-stereo Worldview-3 satellites to produce Digital Elevation Models (DEM). Agisoft Metashape Professional software (Version 2.0, 2021) was used to build a point cloud data set of matched points in each of the images. The dense cloud of point data was then rasterized to build an elevation model of the area. Using the Pléiades satellite imagery, we built an elevation model with 1 m horizontal resolution. The Worldview-3 imagery yielded a DEM with 50 cm horizontal resolution. Additionally, we used legacy Corona imagery from 1967 to observe the ground surface prior to major urbanization of Aşgabat. Faults we mapped remotely using the QGIS software. We identified linear features cross-cutting topography, uphill facing scarps, offset drainages, shutter ridges and offsets in anthropogenic features.

We measured vertical scarp heights across faults remotely from DEMs derived from tri-stereo Pléiades satellite imagery. The precise location of the fault trace projected to the surface is unknown and we defined the fault position at the steepest point on the scarp (Grützner *et al.* 2017a,b; Tsai *et al.* 2022). The scarp profiles were

extracted using the *Terrain Profile* tool in QGIS from the DEMs. The boundaries of the scarps and Quaternary terraces were defined by identifying the apparent changes in curvature. We estimated the best-fitting gradients of the surfaces on both sides of the fault using a least-squares linear regression. The scarp height was defined as the vertical distance between the two fitted gradients (Tsai *et al.* 2022).

3.2 Seismic analysis

The various seismic methods of epicentre location and relocation, and focal mechanism calculation are described in detail in the Section 5. Phase arrival times, relocated event data and P -wave polarity data are detailed in Tables 1–3, respectively.

3.3 Age control

Age control on alluvial fans displaced by faulting came from single grain IRSL dating of feldspar grains, using methods as described in Walker *et al.* (2021). To collect the samples, we dug a 1.2 m sample pit into an uplifted alluvial surface at 38.043°N/58.026°E.

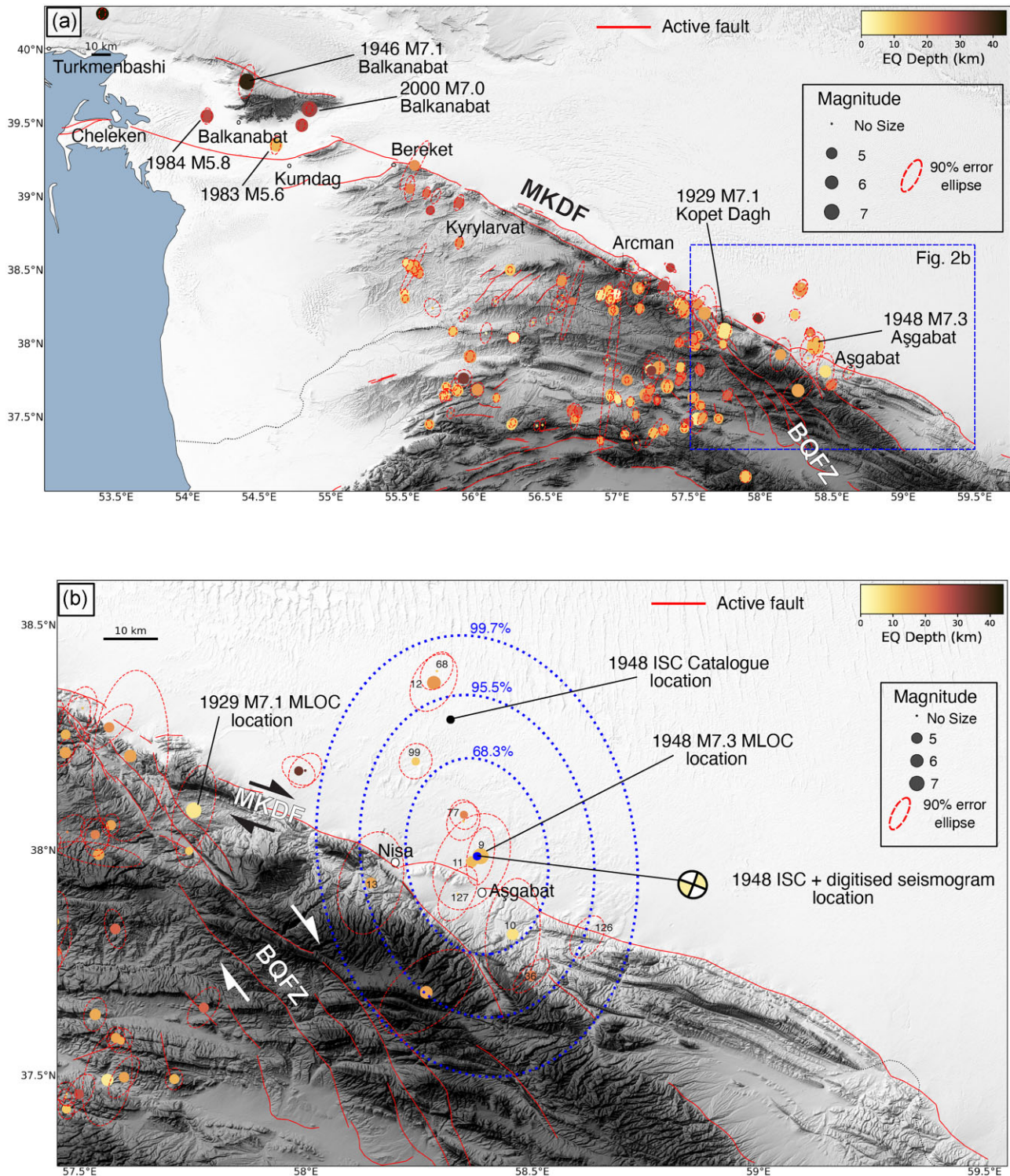


Figure 2. (a) Hypocentral locations of earthquakes between 1929 and 2019 scaled by magnitude with 90 per cent confidence interval (Table 2). Locations are calibrated using the hypocentroidal decomposition technique. The earthquakes are coloured by focal depth. DEM is from SRTM 30 m. (b) Hypocentre location of the 1948 Aşgabat earthquake located using the ISC phase arrival data (blue) (Table 1); the ISC phase arrival data combined with phase arrivals from the digitized waveforms (black) (Table 1); calibrated earthquake location using the hypocentroidal decomposition relative relocation method (a). Dotted blue lines represent confidence intervals showing a measurement of the error in the location. DEM is from SRTM 30 m.

The stratigraphy (bottom to top) consisted of a 20 cm fine grained and silt layer capped by 30 cm of blocky gravels. Above this there is 20 cm compact loess layer with a less well consolidated 50 cm loess

cap. We took two adjacent samples at a depth 100 cm (TK1909 and TK1910) in the fine-sand/silt layer and a further sample (TK1911) at a depth of 55 cm in the compact loess deposit (Table 4).

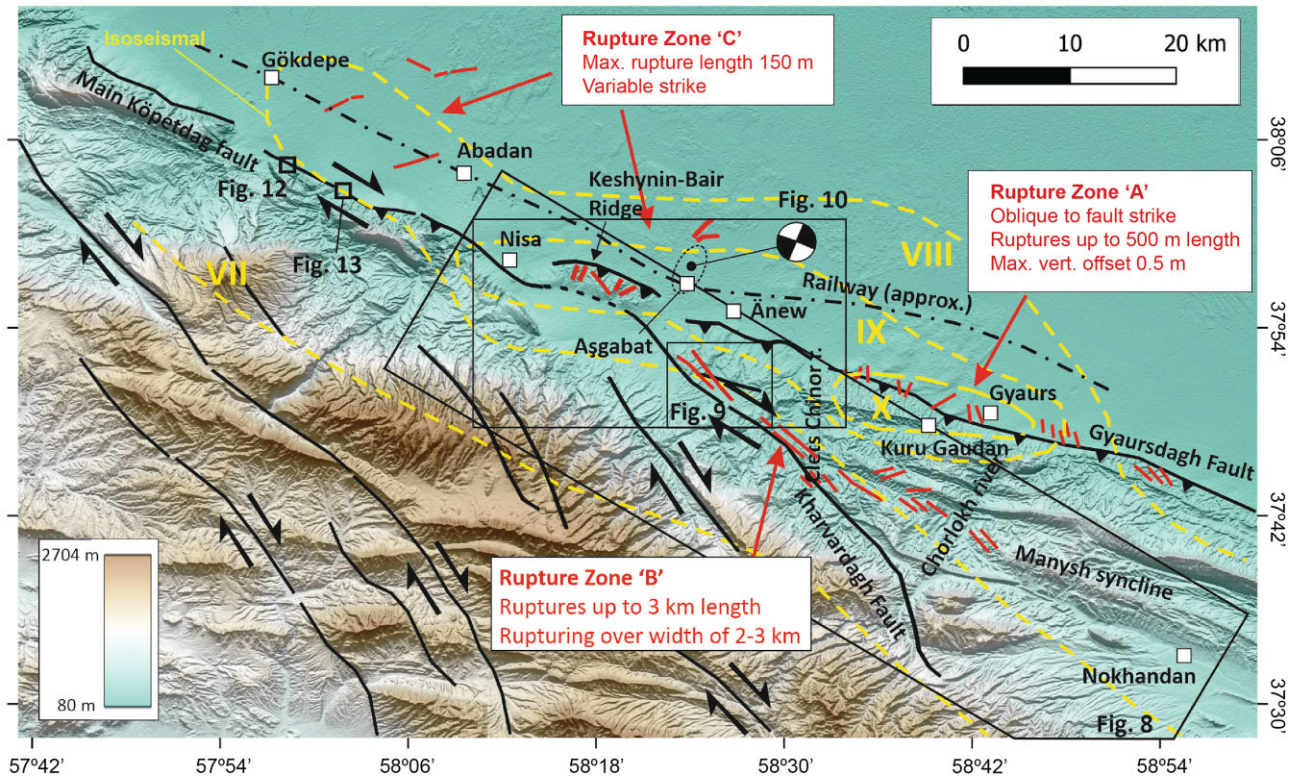


Figure 3. Ashgabat region showing reported earthquake ruptures. Black lines are active faults (mapped by the authors) and red lines are 1948 ruptures digitized from the Gorkoshev 1949 geological study (Rogozhin 1995). Difficulties in georeferencing means that the rupture locations should be used as an approximate guide only. The ruptures are separated into three main areas of rupture (a, b, c). MSK isoseismal contours are from Berberian & Yeats (2001), who combined several the other sources along with their own intensity observations in Iran.

4 THE 5 OCTOBER 1948 AŞGABAT EARTHQUAKE ($M_{7.3}$)

4.1 Overview and macroseismic effects

The M_s 7.3 Ashgabat earthquake occurred at 20:12:07 GMT on the 5 October 1948, corresponding to 01:12 a.m. local time on the 6 October. It was followed by a number of strong aftershocks in the following days, including at 6 a.m. and 10 a.m. local time on the 6 October (as reported by Fedorov 1998), and another on the 8th that caused additional deaths. The Ashgabat seismic station recorded 138 aftershocks over the month from 20 October to 20 November 1948. The main shock largely destroyed the city of Ashgabat and caused heavy damage over a wide region. Within Ashgabat and surroundings there was near total collapse of brick buildings, heavy damage to concrete structures and infrastructure, and the destruction of all medical facilities (Sidorin 2019). All utility networks in the city other than water were rendered inoperable. The city was cut off from the outside world, resulting in considerable delay in activating relief efforts.

The death toll in the earthquake is not known precisely due to a combination of information restrictions in the USSR at that time and imprecise estimates of the immediate post-war population (Sidorin 2019). Estimates vary between 10 000 and 120 000 casualties, with most recent publications suggesting ~40 000 deaths (35 000 in Ashgabat) as the most likely figure (Sidorin 2019). The earthquake and its effects are a major feature within the cultural memory of Turkmenistan. Casualties and damage extended over the border into Iran, with destruction of over thirty villages, and more than 350 people killed in the Darrez Gaz region.

Several isoseismal maps have been published (Sukacheva & Kazanlı 1949; Rezanov 1957; Rustanovich 1967; Golinskiy & Nepesov 1968; Shebalin 1974; Gorshkov 1984; Berberian & Yeats 2001). There are variations between these in the exact shape of the contours, and in the peak intensity. All agree on an overall elongate NW–SE ellipse, with wider contour spacing to the northeast side of the epicentral zone (e.g. Fig. 3). The isoseismal contours are misaligned with the Köpetdag range front, extending into the mountains in the southeast and into the piedmont in the northwest. Irregularities in the shape have been used by Berberian & Yeats (2001) to infer rupture on more than one misaligned fault. Peak intensities of X were recorded at Gyaurdagh and Kuru Gaudan, and IX at Ashgabat, Nisa, and Anew (Fig. 3). Rogozhin (1995) suggests that the large intensities at Kuru Gaudan may be related to site effects, with the water table near to the surface in this region.

4.2 Ruptures and surface deformation

Surface ruptures have been reported in several previous studies, based on observations made in 1948, and contained in reports that are not publicly available (Rogozhin 1995; Sidorin 2019). There are remaining uncertainties in the exact positioning of each reported rupture, but by comparing to our satellite derived DEMs we identify nearby indications of active faulting that we infer to have ruptured in the earthquake.

Ground displacements mapped after the 1948 earthquake occur in three main zones (Rogozhin 2012; Sidorin 2019; Nikonov 1998; Rezanov 1957), extending both northwest (zone C) and southeast (zone B) of Ashgabat and east (zone A) of Ashgabat within the Gyaurdagh

Table 1. Phase arrival times from the 1948 Aşgabat earthquake from a global network of seismometers constructed from the ISC Bulletin database (International Seismological Centre 2022) and the digitized waveforms.

Station	Location	Phase	Arrival time	Digitized
SAM	Samarkand, Uzbekistan	P	20:13:47	N
BAK	Baku, Azerbaijan	P	20:13:51	N
DSH	Dushanbe, Tajikistan	P	20:14:07	N
TAS	Tashkent, Uzbekistan	P	20:14:16	N
KUL	Kulyob, Tajikistan	P	20:14:17	N
CHM	Chimkent, Kazakhstan	P	20:14:23	N
GRO	Groznyy, Russia	P	20:14:44	N
ANR	Andizhan, Uzbekistan	P	20:14:44	N
LEN	Gyumri, Armenia	P	20:14:48	N
ERE	Yerevan, Armenia	P	20:14:49	N
MUR	Murghob, Tajikistan	P	20:15:02	N
PYA	Pyatigorsk, Russia	P	20:15:09	N
FRU	Bishkek, Kyrgyzstan	P	20:15:14	N
DSH	Dushanbe, Tajikistan	S	20:15:38	N
SOC	Sochi, Russia	P	20:15:39	N
AAA	Almaty, Kazakhstan	P	20:15:40	N
TAS	Tashkent, Uzbekistan	S	20:15:56	N
CHM	Chimkent, Kazakhstan	S	20:16:12	N
FEO	Feodosiya, Crimea	P	20:16:24	N
SVE	Sverdlovsk, Russia	P	20:16:25	N
KSA	Ksara, Lebanon	P	20:16:26	N
YAL	Yalta, Crimea	P	20:16:27	N
SIM	Simferopol, Crimea	P	20:16:35	N
ANR	Andizhan, Uzbekistan	S	20:16:47	N
GRO	Groznyy, Russia	S	20:16:52	N
ERE	Yerevan, Armenia	S	20:16:54	N
DDI	Dehran Dun, India	P	20:17:00	N
MOS	Moscow, Russia	P	20:17:07	N
ISK	Istanbul, Turkey	P	20:17:09	N
BOM	Bombay, India	P	20:17:14	Y
HLW	Helwan, Egypt	P	20:17:18	N
CRB	Chernovtsy, Ukraine	P	20:17:25	N
BOM	Bombay, India	PP	20:17:31	Y
PYA	Pyatigorsk, Russia	S	20:17:31	N
BUC	Bucharest, Romania	P	20:17:36	N
FRU	Bishkek, Kyrgyzstan	S	20:17:37	N
CMP	Campulung, Romania	P	20:17:44	N
HYD	Hyderabad, India	P	20:17:50	N
BEO	Belgrade, Serbia	P	20:18:08	N
BUD	Budapest, Hungary	P	20:18:08	N
CAL	Calcutta, India	P	20:18:10	N
WAR	Warsaw, Poland	P	20:18:13	N
SOC	Sochi, Russia	S	20:18:20	N
HEL	Helsinki, Finland	P	20:18:22	N
AAA	Almaty, Kazakhstan	S	20:18:27	N
RAC	Raciborz, Poland	P	20:18:29	N
TAR	Taranto, Italy	P	20:18:29	N
KOD	Kodaikanal, India	P	20:18:40	N
PRA	Prague, Czech Republic	P	20:18:46	N
CAT	Catania, Italy	P	20:18:47	N
TRS	Trieste, Italy	P	20:18:51	N
IRK	Irkutsk, Russia	P	20:18:53	Y
CLL	Collm, Germany	P	20:18:57	N
ROM	Rome, Italy	P	20:18:59	N
COP	Copenhagen, Denmark	P	20:19:03	N
CAL	Calcutta, India	PP	20:19:05	N
BOL	Bologna, Italy	P	20:19:07	N
FIR	Florence, Italy	P	20:19:07	N
COC	Colombo, Sri Lanka	P	20:19:08	N
MES	Messina, Italy	P	20:19:12	N
CHU	Chur, Switzerland	P	20:19:12	N
SAL	Salò, Italy	P	20:19:13	N
POT	Potsdam, Germany	P	20:19:17	Y

Table 1. Continued

Station	Location	Phase	Arrival time	Digitized
DBN	De Bilt, Holland	P	20:19:43	Y
SVE	Sverdlovsk, Russia	S	20:19:54	N
FEO	Feodosiya, Crimea	S	20:19:56	N
KSA	Ksara, Lebanon	S	20:20:07	N
SIM	Simferopol, Crimea	S	20:20:10	N
ALG	Algiers, Algeria	P	20:20:15	N
DDI	Dehran Dun, India	S	20:20:18	N
POT	Potsdam, Germany	PP	20:20:27	Y
ALI	Alicante, Spain	P	20:20:29	N
TAM	Tamanrasset, Algeria	P	20:20:41	N
ABE	Aberdeen, Scotland	P	20:20:46	Y
MOS	Moscow, Russia	S	20:21:07	N
ISK	Istanbul, Turkey	S	20:21:19	N
HLW	Helwan, Egypt	S	20:21:38	N
CRB	Chernovtsy, Ukraine	S	20:21:49	N
BUC	Bucharest, Romania	S	20:21:59	N
AIK	Aikawa, Japan	P	20:22:09	N
OWA	Owase, Japan	P	20:22:19	N
OSA	Osaka, Japan	P	20:22:22	N
KAM	Kameyama, Japan	P	20:22:24	N
HYD	Hyderabad, India	S	20:22:26	N
ABE	Aberdeen, Scotland	PP	20:22:33	Y
KOB	Kobe, Japan	P	20:22:33	N
SAP	Sapporro, Japan	P	20:22:34	N
CAL	Calcutta, India	S	20:22:45	N
BEO	Belgrade, Serbia	S	20:22:54	N
WAR	Warsaw, Poland	S	20:23:04	N
RAC	Raciborz, Poland	S	20:23:12	N
TAR	Taranto, Italy	S	20:23:16	N
BUD	Budapest, Hungary	S	20:23:17	N
HEL	Helsinki, Finland	S	20:23:21	N
KOD	Kodaikanal, India	S	20:23:40	N
COL	College, Alska, USA	P	20:24:00	Y
PRA	Prague, Czech Republic	S	20:24:02	N
COL	College, Alska, USA	P	20:24:03	Y
TRS	Trieste, Italy	S	20:24:14	N
CAT	Catania, Italy	S	20:24:15	N
CLL	Collm, Germany	S	20:24:26	N
MES	Messina, Italy	S	20:24:27	N
COP	Copenhagen, Denmark	S	20:24:35	N
ROM	Rome, Italy	S	20:24:36	N
FIR	Florence, Italy	S	20:24:41	N
BOL	Bologna, Italy	S	20:24:45	N
CHU	Chur, Switzerland	S	20:24:47	N
SAL	Salo, Italy	S	20:24:49	N
COC	Colombo, Sri Lanka	S	20:24:53	N
ABU	Abuyama, Japan	PP	20:24:56	Y
CLE	Cleveland, USA	P	20:25:37	Y
DBN	De Bilt, Holland	S	20:25:38	Y
DBN	De Bilt, Holland	S	20:26:14	Y
BUR	Burlington, USA	P	20:26:19	Y
ALG	Algiers, Algeria	S	20:26:44	N
ALI	Alicante, Spain	S	20:27:09	N
ABE	Aberdeen, Scotland	S	20:27:12	Y
TAM	Tamanrasset, Algeria	S	20:27:30	N
CLE	Cleveland, USA	S	20:29:30	Y
SJP	San Juan, Puerto Rico	PP	20:30:34	Y
SAP	Sapporro, Japan	S	20:30:38	N
KAM	Kameyama, Japan	S	20:30:44	N
OWA	Owase, Japan	S	20:30:46	N
KOB	Kobe, Japan	S	20:30:56	N
OSA	Osaka, Japan	S	20:30:56	N
CHC	Chappel Hill, USA	PP	20:31:21	Y
WEL	Wellington, New Zealand	PKIKP	20:31:58	Y
ABU	Abuyama, Japan	S	20:32:21	Y

Table 1. Continued

Station	Location	Phase	Arrival time	Digitized
ABU	Abuyama, Japan	S	20:32:59	Y
HUA	Huancayo, Peru	PP	20:33:30	Y
ARA	Arapuni, New Zealand	P	20:33:30	N
API	Apia, Samoa	P	20:33:37	Y
CHC	Chappel Hill, USA	S	20:33:39	Y
COL	College, Alska, USA	S	20:33:43	Y
COL	College, Alska, USA	S	20:34:09	Y
WEL	Wellington, New Zealand	Pdiff	20:35:32	Y
LIN	Lincoln, Newbraska, USA	S	20:36:48	Y
BUR	Burlington, USA	S	20:37:18	Y
COL	College, Alska, USA	SS	20:38:39	Y
ABU	Abuyama, Japan	Pdiff	20:39:18	Y
ABU	Abuyama, Japan	Pdiff	20:40:10	Y
ARA	Arapuni, New Zealand	S	20:43:30	N
API	Apia, Samoa	S	20:50:55	Y

anticline near Kuru Gaudan, as shown in Fig. 3. Fractures were also mapped on the Keshenyn-Bair ridge that runs between Aşgabat and Nisa, close to the Ānew mosque, and along the highway ~8 km south of Ānew (Fig. 3). Authors disagree on the extent to which any or all of the dislocations represent primary fault rupture, secondary faulting, or associated fissuring caused by hydrological changes (Rezanov 1957; Rustanovich & Shirokova 1964; Rogozhin 1995; Rogozhin 2012). The rupture zones are discontinuous, but define an overall end-to-end length of ~80 km. None of the rupture zones align with the main range-bounding faults of the Köpetdag, despite careful field checking of these faults by Gorshkov (1948). We provide further interpretation of the surface ruptures and the active faulting below.

The first area of reported rupture (Zone A on Fig. 3) is found east of Aşgabat along the frontal (northern) limb of the Gyaursdag anticline and fault striking WNW–ESE with a concentration of reported ruptures at the village of Kuru Gaudan. The length of this rupture zone is ~40 km, with the individual fractures perpendicular to the roughly east–west strike of the anticline. Individual ruptures are up to 500 m in length and have a maximum vertical offset of 0.5 m (Rezaonov 1957; Rogozhin 2012; Sidorin 2019). A detailed map of one section of these perpendicular fractures near the settlement of Kuru Gaudan, from Tchlenko's personal documents, is shown in Fig. 4. Here, ruptures with relative displacements of up to 1 m form complex stepped horsts and grabens that are up to 1 m wide (Rogozhin 1995). Ejections of sediments and mud volcanoes (up to 20 m in diameter with a height of 0.5 m) were also observed near Kuru Gaudan (Rogozhin 1995; Sidorin 2019), which could be evidence of liquefaction.

Rogozhin (1995) suggests that the fractures observed along the Gyaursdag anticline are gravitational, though the apparently right-stepping arrangement of fractures may indicate a combination of fold growth and right-lateral motion above a blind fault tip, as seen for instance in the 1957 Gobi-Altay earthquake in Mongolia (Kurushin *et al.* 1998). However, this is not clear in the satellite imagery (Fig. 4). Indications of coseismic shortening across the Gyaursdag anticline come from reports of damaged water pipes in several places at Kuru Gaudan, with pipes buckled to heights of 1 m, and the telescoping of one pipeline over a length of 3 m (Butovskaya & Kovalenko 1955).

The second rupture zone (Zone B) coincides with the Kharvardagh geological fault zone and is orientated NW–SE. It begins ~5 km southeast of Aşgabat and extends further southeast for a

distance of ~35–40 km within the Manysh syncline (Fig. 3). Reported individual rupture lengths range from several hundred meters in the west to 3 km across a 2–3 km wide zone (Rogozhin 1995; Sidorin 2019). Rogozhin (1995) separates the ruptures into north and south zones. The northern one is ~6 km in total length, beginning near the headwaters of the Celts-Chinor river (Fig. 3). The southern one extended a further 15 km to the southeast, ending at the headwaters of the Chorlokh river (Fig. 3). The NW–SE ruptures tracked across undulating topography caused by multiple minor northeast-flowing drainages. Along the northern section upslope-facing scarps ~0.5 m high formed to the northern sides of the valleys, potentially suggesting lateral displacement of topography.

The third zone of rupturing (Zone C in Fig. 3) occurs northwest of Aşgabat in a low relief area north of the Köpetdag range front. Individual ruptures (cracks) were short (<150 m) in length and discontinuous (Rogozhin 1995; Sidorin 2019), with trends of 0°, 60°–70°, 90° and 300°. The ruptures are described as consisting both of fissures up to 30–40 cm wide and with a vertical displacement of up to 20–30 cm, and compressive features accompanied by warping of the ground and eruptions of mud. Rogozhin (1995) and others have suggested that these ruptures are associated with local geological conditions such as a groundwater and swelling of sediment and mud volcanoes.

Post-earthquake resurveying of the Trans-Caspian railroad (approximate route shown in Fig. 3) provides an additional constraint on surface deformation at various points within the epicentral zone. Re-levelling revealed varying vertical displacements, ranging from 22 cm of subsidence at Ānew (Anau) east of Aşgabat (Butovskaya & Kovalenko 1955; Rezanov 1957; Kolibacv 1962), to uplift of 33 cm at Büzmeýin (Bezmein/Abadan) west of Aşgabat. Within Aşgabat itself the levelling data shows almost pure right lateral displacement of 178–190 cm.

4.3 Published source parameters from seismology

Published focal mechanisms of the 1948 earthquake show predominantly reverse faulting striking 110°–290°, with one nodal plane nearly vertical with uplift to the north, and the other plane nearly horizontal plane indicating thrusting of the southern block to the NNE (Rustanovich & Shirokova 1964; McKenzie 1972). The focal mechanism has been used to suggest predominantly thrust motion

Table 2. Earthquake catalogue showing the location, depth and magnitude of relocated events using the MLOC method of hypocentroidal decomposition.

Number	Date	Time	Latitude	Longitude	Depth (km)	Magnitude
1	01/05/1929	21:17:32	38.0901	57.75175	6	7.1
2	03/05/1929	16:20:04	37.99202	57.54186	15	5.1
3	13/05/1929	13:27:12	37.83842	57.29086	15	5.8
4	13/07/1929	07:36:40	37.6855	58.2657	15	5.7
5	25/07/1929	00:17:26	38.21068	57.61191	15	5.6
6	19/09/1939	03:24:05	38.38081	57.14887	15	5.6
7	04/11/1946	21:47:49	39.78535	54.41388	41	7.1
8	18/06/1948	18:44:33	37.49156	57.56102	5	5.5
9	05/10/1948	20:12:06	37.98799	58.38585	12	7.3
10	06/10/1948	01:24:43	37.81474	58.45691	7	5.3
11	06/04/1950	02:43:30	37.9758	58.36648	12	5
12	09/05/1950	11:16:58	38.37312	58.28216	17	6.2
13	15/09/1952	04:31:31	37.92868	58.14308	15	4.9
14	12/02/1964	08:19:18	39.21631	55.58492	18	4.7
15	02/01/1966	16:33:07	37.83356	56.95344	10	
16	18/01/1966	20:54:11	37.82239	57.00199	20	
17	03/01/1969	03:16:38	37.09915	57.89763	11	5.4
18	30/07/1970	00:52:18	37.91641	55.97292	17	5.7
19	30/07/1970	02:35:11	37.76736	55.92736	33	4.9
20	30/08/1970	16:17:30	37.69081	56.02371	17	5
21	12/11/1970	13:10:02	38.39853	57.32867	29	4.7
22	12/10/1972	10:26:09	38.28453	56.58716	12	
23	07/03/1974	11:36:00	37.68516	55.88506	10	5.2
24	14/02/1976	15:29:51	37.68933	57.23338	19	4.2
25	31/05/1976	08:07:13	38.96327	55.89629	25	4.8
26	14/06/1978	16:25:31	38.04499	56.27835	5	4.9
27	08/03/1979	22:40:33	37.45993	57.4981	27	4.5
28	06/10/1979	11:55:44	38.27415	57.5647	18	4.6
29	14/03/1983	12:12:45	39.35403	54.61675	12	5.6
30	22/02/1984	05:44:40	39.55186	54.13543	28	5.8
31	21/08/1984	19:48:49	38.33267	56.88419	5	4.6
32	05/09/1984	18:50:39	38.36245	56.93677	10	4.7
33	05/09/1984	11:19:11	38.34002	56.99391	0	4.4
34	09/05/1985	14:08:34	38.26755	56.61431	15	
35	01/12/1985	20:31:47	37.55327	56.68497	23	4.7
36	05/07/1987	07:43:04	37.72232	58.49802	21	4.8
37	07/09/1987	11:32:26	39.48895	54.79772	28	5.7
38	31/05/1992	16:39:24	38.68921	55.89864	19	4.4
39	09/09/1992	19:27:34	37.39613	57.25546	11	4.7
40	06/10/1992	08:57:18	38.43091	56.61419	17	4.7
41	06/01/1993	17:16:53	37.49751	57.59755	15	4.7
42	18/02/1993	04:15:01	37.65182	57.77365	24	4.5
43	02/05/1993	04:26:38	39.05774	55.55226	20	4.5
44	01/07/1994	10:12:41	40.24923	53.404	44	5.6
45	16/10/1994	10:09:54	38.51942	57.37345	28	3.9
46	21/10/1994	11:46:24	38.32201	56.99406	10	4.8
47	04/02/1997	10:37:48	37.71772	57.35096	18	5.9
48	04/02/1997	09:53:56	37.70851	57.35052	11	5.4
49	04/02/1997	21:04:12	37.81947	57.23981	32	4.1
50	05/02/1997	07:53:46	37.63656	57.53406	14	5.1
51	18/02/1997	18:01:36	37.84267	57.44368	10	4.2
52	22/08/2000	16:55:14	38.21793	57.46804	15	5.1
53	01/09/2000	05:04:46	38.25852	57.46846	13	4.4
54	19/09/2000	15:19:09	38.27794	57.43474	8	4.7
55	06/12/2000	17:11:06	39.60021	54.85161	30	7
56	11/09/2003	14:00:34	37.82656	57.23012	4	4.5
57	21/08/2004	03:32:43	37.82644	57.5782	24	4.7
58	17/08/2005	20:55:26	38.03617	57.53407	20	4.2
59	10/09/2005	01:10:03	38.3422	57.38418	20	
60	16/09/2006	10:42:54	37.49312	57.70862	13	4.4
61	29/11/2006	21:38:49	37.51892	57.1317	15	3.5
62	20/04/2007	08:04:41	37.54408	56.7299	25	3.9
63	19/08/2007	13:45:35	38.53637	55.5894	22	4.3
64	20/08/2007	04:53:31	37.77651	57.44823	22	4.6

Table 2. Continued

Number	Date	Time	Latitude	Longitude	Depth (km)	Magnitude
65	01/10/2007	03:07:08	37.44936	56.47985	10	
66	29/02/2008	19:57:40	38.24187	57.15867	15	4.4
67	01/08/2008	22:44:38	37.45504	55.68835	12	4.3
68	01/08/2008	21:13:54	38.39899	58.28896	10	
69	14/10/2008	01:59:03	37.48624	56.70201	13	
70	24/10/2008	05:14:15	38.23795	57.37276	10	
71	06/02/2009	18:14:29	38.01086	57.43507	20	4.3
72	17/02/2009	17:57:23	38.29408	56.68847	22	3.3
73	17/02/2009	18:03:34	38.33147	56.6185	10	
74	21/02/2009	21:45:26	38.04246	57.47209	20	
75	15/04/2009	07:54:01	37.6506	55.81009	10	3.2
76	11/09/2009	20:53:01	37.75063	57.43499	23	3.5
77	31/12/2009	23:16:38	38.08044	58.34872	20	3.5
78	19/04/2010	03:31:13	37.49287	56.70936	15	4.4
79	25/05/2010	13:03:19	38.17759	57.98372	35	4
80	30/05/2010	08:48:39	38.17834	57.99821	35	
81	23/07/2010	00:56:41	37.658	56.95659	13	4.8
82	08/08/2010	09:39:01	37.99966	57.74134	10	3.5
83	11/08/2010	17:26:19	37.75608	57.06982	17	5
84	18/10/2010	08:05:11	38.07559	56.08548	2	
85	15/05/2011	14:49:36	37.64743	55.78103	8	3.4
86	17/06/2011	19:55:40	37.64211	56.95522	8	4.2
87	17/06/2011	20:07:59	37.62512	57.00528	5	3.6
88	08/11/2011	20:11:12	37.65777	55.8245	5	
89	09/11/2011	01:20:39	37.71071	55.8061	9	4.2
90	13/11/2011	12:30:38	37.65051	55.79393	7	
91	26/12/2011	01:49:13	37.58472	57.57978	15	4.5
92	26/12/2011	03:25:42	37.57852	57.59052	14	3.4
93	03/02/2012	19:07:33	38.08671	55.85415	10	4.3
94	10/03/2012	15:54:28	37.32906	57.13464	10	
95	16/04/2012	04:22:21	37.38562	57.05462	10	3.9
96	19/04/2012	18:01:01	37.39816	57.06686	20	
97	08/09/2012	03:17:36	38.50429	55.60953	14	4.2
98	09/09/2012	06:46:16	38.53659	55.55283	11	3.6
99	22/09/2012	12:27:15	38.19883	58.24226	10	3.6
100	01/10/2012	08:43:49	38.54086	55.57427	13	4.4
101	01/10/2012	08:51:16	38.53371	55.59461	14	4
102	01/10/2012	14:36:11	38.49605	55.58938	14	
103	02/10/2012	20:19:49	38.51954	55.55249	13	4.2
104	23/02/2013	23:12:33	38.90967	55.69564	28	4
105	28/02/2013	11:06:02	38.05756	57.56878	15	4.5
106	30/04/2013	02:00:12	37.42845	57.33484	12	3.6
107	10/05/2013	15:55:09	37.40632	57.3211	20	3.9
108	01/07/2013	01:36:01	38.06575	58.34774	11	
109	09/12/2013	11:33:51	38.51677	55.59254	10	5.1
110	09/12/2013	23:19:45	38.49048	55.59273	15	4
111	10/12/2013	03:42:32	38.51539	55.5783	15	3.6
112	13/02/2014	08:35:50	38.5055	56.25343	10	4.8
113	10/04/2014	00:08:43	38.51957	55.57716	24	4.2
114	10/04/2014	23:13:57	38.47823	55.62252	16	3.3
115	16/04/2014	05:27:40	38.17813	56.53517	10	
116	21/04/2014	02:35:58	37.46672	56.27517	10	3.9
117	12/10/2014	00:24:14	37.34481	56.88379	15	3.4
118	27/10/2014	21:00:35	37.45186	56.26208	8	4.4
119	19/05/2015	01:45:17	38.55509	55.52408	6	3.4
120	30/05/2015	06:19:23	38.31671	57.50594	12	
121	31/05/2015	12:10:14	38.24747	55.71141	12	
122	12/10/2015	21:37:30	38.23119	56.97518	14	4.8
123	12/10/2015	21:52:47	38.29753	56.94529	7	
124	13/10/2015	17:26:23	38.33641	56.95049	6	
125	16/11/2015	17:03:12	38.30452	56.95245	9	4.1
126	19/12/2015	19:10:04	37.80859	58.62128	7	
127	02/03/2016	16:07:05	37.90475	58.3354	10	
128	04/03/2016	14:57:25	38.29113	56.15072	10	
129	26/03/2016	23:51:01	38.14846	56.41316	10	

Table 2. Continued

Number	Date	Time	Latitude	Longitude	Depth (km)	Magnitude
130	29/06/2016	22:56:13	37.45244	57.46855	14	
131	14/07/2016	08:35:40	37.4267	57.47044	10	4
132	05/11/2016	18:32:33	37.72421	55.86583	7	
133	09/11/2016	04:17:05	39.00581	55.73548	30	
134	26/01/2017	02:24:48	38.37943	57.16299	8	
135	06/02/2017	23:37:18	38.21004	55.94796	10	
136	07/02/2017	00:29:01	38.19152	55.92797	10	
137	14/03/2017	04:05:21	38.34476	55.5148	5	4.1
138	16/03/2017	00:48:25	37.53072	55.83747	20	
139	19/03/2017	14:55:30	38.30881	55.52077	12	4
140	13/05/2017	18:00:59	37.65444	57.19932	14	5.5
141	14/05/2017	02:59:45	37.62543	57.28129	15	
142	19/05/2017	11:27:26	37.61425	57.27928	23	3.3
143	02/07/2017	20:50:17	39.02745	55.66965	23	3.7
144	10/07/2017	07:04:54	38.03046	57.53785	18	
145	14/09/2017	09:38:18	38.41989	57.19935	15	
146	02/10/2017	05:35:07	37.63363	56.15776	12	3.6
147	10/10/2017	17:02:19	37.45974	57.47114	10	
148	17/10/2017	18:52:37	37.63624	57.21016	22	4.6
149	17/11/2018	05:21:15	37.60644	57.09352	10	3.8
150	10/04/2019	16:17:48	37.89286	56.93078	6	
151	22/05/2019	01:52:17	37.4455	56.44118	8	
152	29/07/2019	09:27:46	38.52742	57.11668	6	

Table 3. Polarity data used to calculate focal mechanism solutions from the first arrival data. The table shows if the record has come from digitized seismograms or/and from the ISC catalogue (International Seismological Centre 2022). Station locations are taken from Charlier & Van Gils (1953), and International Seismological Centre (2022). Take-off angles are calculated using Pho & Behe (1972).

Station	Location	Latitude	Longitude	ISS/ISC Catalogue	Digitized waveform	Take-off angle	Compression/dilation
BOM	Bombay, India	18.90	72.82	N	Y	34	D
ISK	Istanbul, Turkey	41.07	29.06	Y	N	32	C
HLW	Helwan, Egypt	29.86	31.34	Y	N	31	C
BEO	Beograd, Serbia	44.81	20.47	Y	N	29	C
WAR	Warsaw, Poland	52.24	21.02	Y	N	29	D
CAL	Calcutta, India	22.54	88.33	Y	N	29	D
HEL	Helsinki, Finland	60.18	24.96	Y	N	29	D
POT	Potsdam, Germany	52.38	13.07	Y	N	28	D
ROM	Rome, Italy	41.90	12.51	Y	N	28	C
COP	Copenhagen, Denmark	55.69	12.43	Y	N	28	D
POT	Potsdam, Germany	52.38	13.07	N	Y	28	D
BOL	Bologna, Italy	44.49	11.33	Y	N	27.5	D
GTT	Göttingen, Germany	50.55	9.97	N	Y	27.5	D
CHU	Chur, Switzerland	46.85	9.54	Y	N	27	D
STU	Stuttgart, Germany	48.77	9.20	Y	N	27	D
ZUR	Zurich, Switzerland	47.37	8.58	Y	N	27	D
DBN	De Bilt, Netherlands	52.10	5.18	Y	Y	27	D
UCC	Uccle, Belgium	50.80	4.36	Y	N	26.5	D
ABE	Aberdeen, Scotland	57.17	-2.10	N	Y	26	D
TAM	Tamanrasset, Algeria	22.79	5.52	Y	N	25	C
CRT	Cartuja, Spain	37.19	-3.60	Y	Y	24.5	C
UPP	Uppsala, Sweden	59.86	17.63	Y	Y	24	D
LIS	Lisbon, Portugal	38.72	-9.15	Y	N	23.5	C
ABU	Abuyama, Japan	34.87	135.57	N	Y	22	C
COL	College, Fairbanks, USA	64.86	-147.82	N	Y	18	C
OTT	Ottawa, Canada	45.39	-75.72	Y	N	15	D
BUR	Burlington, USA	44.47	-73.19	N	Y	15	C
CLE	Cleveland, USA	41.49	-81.53	Y	Y	14	D
CHC	Chapel Hill, USA	35.90	-79.05	N	Y	14	D

in the earthquake, though the nodal planes are not well constrained, particularly for the very gently south-dipping plane (Jackson & Mackenzie 1984).

Aftershock studies using temporary seismic networks were carried out in June–October 1949 and in June–September 1953 (Rustanovich 1967), revealing concentrations at Kuru Gaudan and at

Table 4. Infrared stimulated luminescence results from sediments taken from terrace site at 38.043°N/58.026°E. A 1.2 m sample pit was excavated in the Q5 surface (Fig. 12), sediments were sampled at depths above.

Field code	Lab code	Depth (m)	Sediment		Sediment U ($\mu\text{g g}^{-1}$)	Sediment Th ($\mu\text{g g}^{-1}$)	Dose rate (mGy yr^{-1})	1σ Uncertainty	Equivalent dose (Gy)	1σ Uncertainty	Age (kyr)	1σ Uncertainty
			K (per cent)									
T19-09	20102	1.00	1.20	1.81	6.10	2.70	± 0.11	9.75	± 2.34	2.80	± 0.23	
T19-10	20103	1.00	0.70	1.07	3.70	1.95	± 0.08	200.1	± 19.8	102.7	± 11.2	
T19-11	20104	0.55	1.40	2.27	7.50	3.08	± 0.13	304.3	± 30.6	98.8	± 11.0	

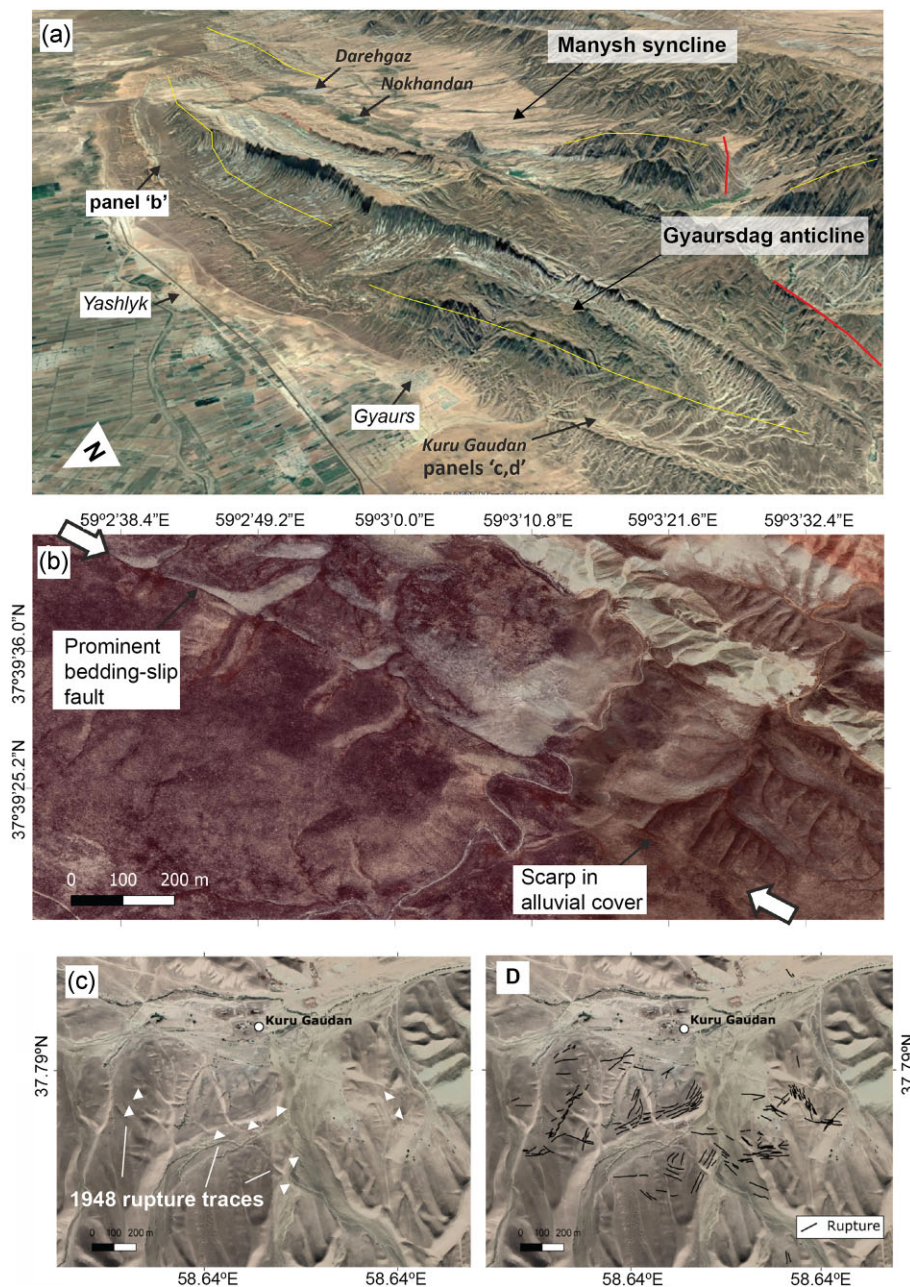


Figure 4. (a) Oblique view to the ESE from a viewpoint above Asgabat (Fig. 3) showing the Gyaursdag anticline in the foreground and the Manysh syncline behind. The axis of the Gyaursdag fold are shown in yellow, and the Kharvardagh right-lateral fault in red. (b) Apparent bedding-slip thrusts within the northern limb of the Gyaursdag fold near Yashlyk. (c and d) Satellite image of Kuru Gaudan showing ruptures associated with the 1948 earthquake (Tchalenko, personal communication).

Bezmein, near the SE and NW ends of the zone of maximum destruction. The majority of aftershocks occurred at depths of 10–12 km. We provide epicentres of larger aftershocks and seismicity in Section 5.2 (Table 2).

5 RE-ANALYSIS OF THE 1948 EARTHQUAKE

5.1 Collection and digitization of seismic records

Our analysis of the Ashgabat earthquake involved the collection, digitization and analysis of seismic data from bulletins and seismograms. The International Seismological Centre (ISC) online bulletin (<http://www.isc.ac.uk/iscbulletin/>) records 175 stations reporting phase arrivals for the 1948 Ashgabat earthquake (International Seismological Centre 2022). However, due to war damage, fire, misplacement and untracked lending over the decades following the event (Okal 2015), it is no longer possible, to recover all the original records. We collated phase arrival information from ISS bulletins (<http://www.isc.ac.uk/iscbulletin/>) and recovered original seismograms for the 1948 earthquake from 21 stations of which 18 are usable (Fig. 5) due to the quality of the record and companion metadata. The azimuthal distribution shows a good level of coverage to the NW but this is poor in the southern hemisphere. We have been unable to obtain seismogram records from neighbouring countries, and the only station in Turkmenistan at that time was destroyed in the earthquake (Sidorin 2019). All arrival time data is presented in Table 1.

We digitized scanned paper seismograms using the same process as detailed in Ou *et al.* (2020). We first digitize the waveforms by tracing over the recorded signal by hand as a Bezier curve in version 2.10 of the GNU Image Manipulation Program (<https://www.gimp.org>). We begin the trace at the minute mark 3 min prior to the first arrival and cease when the waveform can no longer be traced due to saturation, the trace breaks due to dislocation of the stylus or at the edge of the seismogram if the trace cannot be reliably joined. We account for differences in resolutions of the scanned seismograms with the methods used in Ou *et al.* (2020) and Kulikova & Krüger (2015). The seismograms are recorded on different instruments and due to the mechanical designs of these instruments, corrections for geometrical artifacts such as curvature and slant have been made consistent with the methods detailed in Ou *et al.* (2020) and Kulikova & Krüger (2015). We use the same inversion algorithm developed at the University of Potsdam (see Kulikova & Krüger 2015) to restore the symmetry of the waveforms. We collate the instrument parameters, station location and altitude (detailed in Table 3) from the seismograms, station bulletins and from data in Charlier & Van Gils (1953). Where the damping constant or ratio was not available in the literature, we calculate this from the calibration pulse at the start of the seismogram. If there was no such pulse, we chose a best estimate of the most common damping constant or ratio for that particular instrument from Charlier & Van Gils (1953).

5.2 Epicentral location

To improve the location of the 1948 earthquake, and others in nearby parts of Turkmenistan, we use a relocation method based on the hypocentroidal decomposition (HD) approach for multiple event relocation (Jordan & Sverdrup 1981), but extended to develop calibrated locations (minimally biased by unknown Earth structure,

with credible uncertainties) with suitable data sets (Bergman *et al.* 2022). The HD algorithm separates the relocation problem into two parts, with iteration between the two inversions. First, vectors describing the relative locations in space and time of each event in the cluster are determined relative to the hypocentroid, or geometrical centre of the cluster. Secondly, the hypocentroid itself is located. The cluster vectors are then added to the new hypocentroid to obtain updated coordinates for each event. The method has been applied to over 300 clusters of earthquakes worldwide (Bergman *et al.* 2022) and in many individual studies, for example Walker *et al.* (2011), Hayes *et al.* (2013), Mackey & Bergman (2014), Yeck *et al.* (2016) and Karasozen *et al.* (2019). We use a cluster of 152 recorded earthquakes in the calibrated location analysis, detailed in Table 2.

We independently determined the 1948 epicentre from bulletin arrival times and phase arrivals picked from digitized waveforms. We picked arrival times for P, PP, PPP, S, SS and SSS phases from the digitized waveforms using the Snuffler module of the Pyrocko application toolbox (Heimann *et al.* 2017). We prioritized arrival times picked from the vertical component (*Z*) if available and chose the arrival time picked from the horizontal component better oriented to record a given phase from records from other stations. Once we have picked the phase arrivals, we use version 6.0c of the Hyposat inversion algorithm (Schweitzer 2001) to calculate the location of the hypocentre based on the Crust 1.0 and AK135 velocity models (Kennett *et al.* 1995; Laske *et al.* 2013). The algorithm uses first arrival times and time travel differences to iterate a best-fitting hypocentre and phases showing higher residuals were iteratively removed (greater than 30 s) from the calculation, consistent with the methods in previous studies by Ou *et al.* (2020) and Kulikova & Krüger (2017). We calculate three inversions independent of each other. The first uses phase arrival times from the ISC catalogue, the second uses a combination of phase arrival times we picked and the ISC data set. The differences in epicentral location are shown in Fig. 2(b).

Combining the phase arrival times from the digitized waveforms and the ISS bulletin data we calculate, using a 1-D velocity model, a new hypocentre of the 1948 Ashgabat earthquake. Due to the trade-off between onset time and depth we have calculated hypocentres at a variety of depths and show results at different confidence intervals. Fig. 2(b) shows the epicentral locations and HD calibrated relocation with the error ellipses at different confidence intervals. The results show the possible locations of the hypocentre within three confidence intervals at 1, 2 and 3 standard deviations away from the centre at a fixed depth of 12 km, within the error bounds of a floating result. A fixed depth at 12 km is taken from the depth estimate from the HD calibrated results that provide better depth resolution than the 1-D location results.

The calibrated HD hypocentre is also plotted showing the horizontal error with a confidence interval of 90 per cent. We show relocated earthquake hypocentres from 1929 to 2019 (Fig. 2) in the eastern South Caspian region. The cluster locations were calibrated using Iranian seismic network data. The inclusion of calibration data from the south only may produce an unknown amount of bias in the location.

5.3 Focal depth

In the calibrated relocation analysis using MLOC, focal depths may be treated as a free parameter if the arrival time data set includes readings at epicentral distances that are comparable to the focal depth and if such data is available for all or most of the events

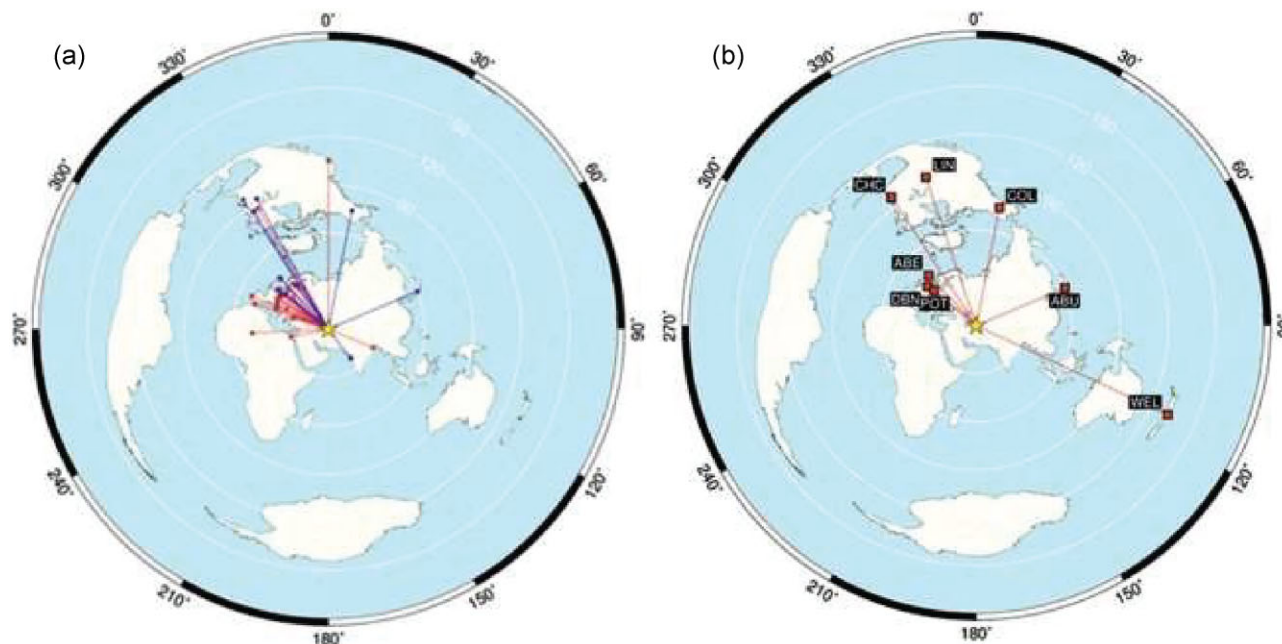


Figure 5. (a) Global coverage of first motion data from ISC records and ISS bulletins (red) and from waveforms digitized within this study (blue). Dots represent the station location, with lines showing the azimuth from the event. (b) Global coverage of stations that have digitized waveforms used for amplitude ratio focal mechanism calculation.

in the cluster. This is rarely the case, so most calibrated clusters are based on focal depths set manually and fixed for the relocation. Focal depths may be set by several means, depending on the specific composition of an event's arrival time data set. Many events have no suitable data to constrain focal depth and must be set at some default value if they are to be included in a calibrated cluster. For the Aşgabat cluster, which includes several very old events, there is a wide range of circumstances. For the 10 events prior to 1950 focal depths for five are constrained by teleseismic depth phases and the other five are set at a default value of 15 km. More recent events all have depth constraint, mainly from arrival time data at near-source or local-distances, with uncertainties of 3–4 km. Eleven events have depth constraint from teleseismic depth phases, and one (20001206.1711, $7.0M_w$) from waveform modelling.

The analysis of teleseismic depth phases is based on the method developed by E.R. Engdahl for the well-known EHB catalogue (Engdahl *et al.* 1998) with the addition of statistical testing that helps identify outlier readings (of which there are many) and provides a quantitative asymmetric estimate of depth uncertainty. For the 1948 Aşgabat main shock the depth of 12 km is based on 9 consistent depth phases (7 were dropped as outliers) that yield an uncertainty of 6 km deeper and 4 km shallower.

5.4 Focal mechanism calculation

We first calculate focal mechanism solutions from the first motion polarity of P -wave arrivals (Fig. 6). Compressional and dilatational arrivals are derived from both the ISC records of ISS bulletins (<http://www.isc.ac.uk/iscbulletin/>) and from the seismogram digitizations on a lower hemisphere projection (Fig. 4). From historical station location records (Charlier & Van Gils 1953; <http://www.isc.ac.uk/iscbulletin/>), we calculated ray path backazimuths for the ray paths and find take-off angles from seismic tables from Pho & Behe (1972). We use the Mtfite software to find nodal plane solutions from the first motion data (Pugh & White 2018).

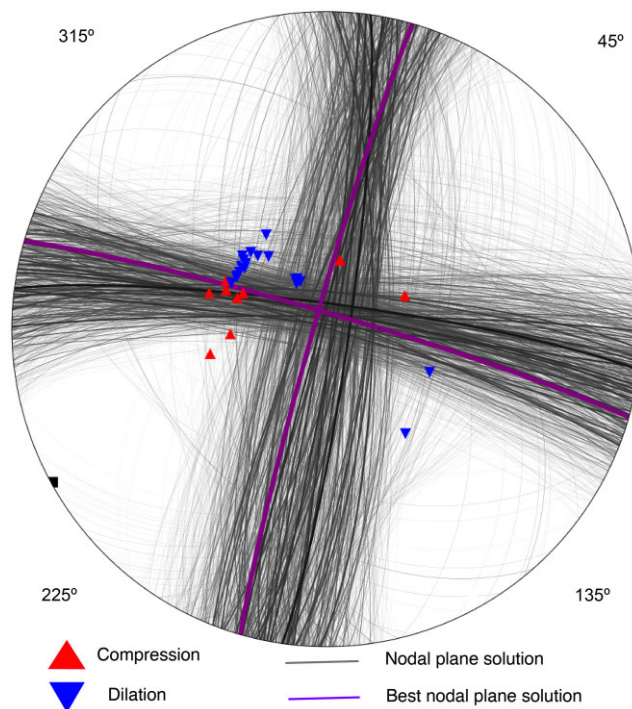


Figure 6. Focal mechanism beach-ball lower hemisphere projection for first motion polarities of P -wave arrivals. Blue triangles are compressions; Red triangles are dilations; grey nodal planes are a random sample of 1000 of the top 1 per cent of results from the Bayesian inversion; purple nodal plane represents the best fit.

Mtfite uses a probabilistic Bayesian earthquake source mechanism inversion approach developed by Pugh *et al.* (2016) to estimate moment tensor solutions. In this study, we constrained the inversion to be double-couple (DC) using first-motion polarity observations

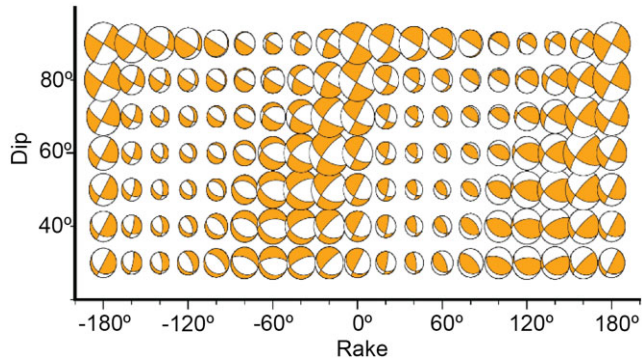


Figure 7. Amplitude ratio focal mechanism results with fixed strike at 120° and depth at 12 km. Dip and rake are calculated at 10° and 20° increments, respectively. The mechanisms are scaled by the misfit to the model, with larger mechanisms having the lowest misfit.

only. We qualitatively weight the uncertainty of the first motion data based on the quality information in the ISS bulletin and the quality of the first arrival in the digitized waveform. This provides a DC-constrained moment tensor solution with an estimate on the uncertainty of the orientation of the nodal planes.

In Fig. 6 we show the first motion data (from Table 3) plotted on a lower hemisphere projection with the most likely 1000 nodal plane solutions from the top 1 per cent of results from the Bayesian inversion (Fig. 3). The results show that the earthquake is most likely to be a strike-slip event. The nodal planes show that strike is most likely to be at either 120° or 30°, for right-lateral and left-lateral slip, respectively, and there is good constraint on the 120° nodal plane. Three of the four stations in the eastern hemisphere of the plot are from the digitized waveforms and we have a higher level of confidence in the polarities of the first motions from this data. For stations where we have both a digitized seismogram and an ISS record of the first motion, we recorded agreement in all cases.

In addition to using first motion polarities, we also determined focal mechanism solutions by fitting the radiation pattern in terms of the ratio between *P*- and *S*-phase amplitudes (Fig. 7). We used the method detailed in Ou *et al.* (2020) modified for our station network distribution and instrument components. We performed a grid search through strikes between 20° and 180°, dips between 20° and 90° and rakes between −180° and 180°. We varied the depth between 10 and 20 km to establish the depth sensitivity of the results and fixed a depth at 12 km from the depth determined for the calibrated hypocentre using the MLOC method. Fig. 7 shows the best-fitting strike, dip and rake for a centroid depth of 12 km. We also fixed strike at 120° taken from the first motion focal mechanism solution. This is within trend of the main faulting in this region (Rogozhin 1995; Walker *et al.* 2021).

The focal mechanisms in Fig. 7 are sized inversely proportional to the misfit between the result and the model, with the largest mechanisms having the smallest misfit. The best solution from this analysis also shows that the mechanism is most likely to be strike-slip. However, due to the coverage of usable waveforms (Fig. 5b) we cannot constrain the dip. The rake shows better constraint with the best solutions occurring at 160° to 180° or −20° to 0° depending on whether this event is left- or right-lateral.

5.5. Magnitude determination

Previous studies calculate a surface-wave magnitude of 7.3 (Shebalin & Tatevossian 1996). We estimate m_B and M_w following

Bormann (2012) and Bormann & Saul (2008) using the following equations:

$$m_B = \log \left(\frac{A_H}{T} \right)_{\max} + Q(\Delta), \quad (1)$$

$$M_w = 1.33m_B - 2.36 \quad (2)$$

where A_H is the vectorially combined horizontal phase amplitude in μm and T is the corresponding period in s. Δ is the epicentral distance, and Q is a distance- and phase-dependent calibration value tabulated in Gutenberg & Richter (1956).

We use the five stations that have vertical components from our digitized catalogue and measure A_H and T from the *P* and *PP* phases. This yields an estimate of $m_B = 7.26 \pm 1.0$ and $M_w = 7.29 \pm 1.4$. The high levels of uncertainty in our magnitude estimates reflect data quality issues with instrument parameters. As a result, we decided not to perform moment magnitude (M_w) calculation using waveform modelling as in Kulikova & Krüger (2015), Kulikova *et al.* (2016, 2017) and Ou *et al.* (2020).

6 TECTONIC GEOMORPHOLOGY

We combined the seismic analyses and contemporary studies of surface rupture and intensities from the 1948 earthquake with an investigation of the tectonic geomorphology of the Ashgabat region, using archive Corona satellite imagery from 1967, modern high-resolution satellite imagery, and derived DEMs to identify active faults from their expression in the landscape. This analysis allowed us to identify potential causative faults of the 1948 earthquake, and to identify fault traces that do not appear to have ruptured the surface. The analysis allows us to better understand the tectonic context of the Ashgabat region, as well as to identify and characterize faults that pose continuing risk to the city and nearby regions. We characterized the active faulting in the area south and east of Ashgabat, in which 1948 earthquake ruptures were reported, both within the city itself and along the range front adjacent to Bezmeim (Abadan) to the west of Ashgabat.

6.1. Gyaursdag anticline

Surface displacements were mapped within the northern limb of the Gyaursdag anticline (Figs 3 and 4). The Gyaursdag anticline is asymmetric, with its core sited close to its northern margin. This arrangement is suggestive of a fault-related fold forming due to slip above a south-dipping thrust fault. No discrete fault scarps are visible at the northern edge of the fold, suggesting that the underlying thrust tip is buried. The preservation of both fold limbs is also strong corroborating evidence that the fault does not reach the surface.

Prominent south-facing scarps are visible in satellite imagery along the northern fold limb (e.g. Fig. 4b). These scarps run parallel to north-tilted bedding in basin sediments, and are visible also in young alluvial materials. We interpret them as bedding slip faults resulting from fold growth (e.g. Cooke & Pollard 1997; Nicol & Nathan 2001). The mapped 1948 ruptures (Fig. 3) show an en-echelon arrangement that may represent a lateral component of slip, suggestive of a tectonic origin. However, the detailed example from Kuru Gaudan shown in Figs 4(c) and (d) show correlation between the locations of the surface deformation and the local topography, suggesting that they may relate, in part, to secondary deformation caused by shaking.

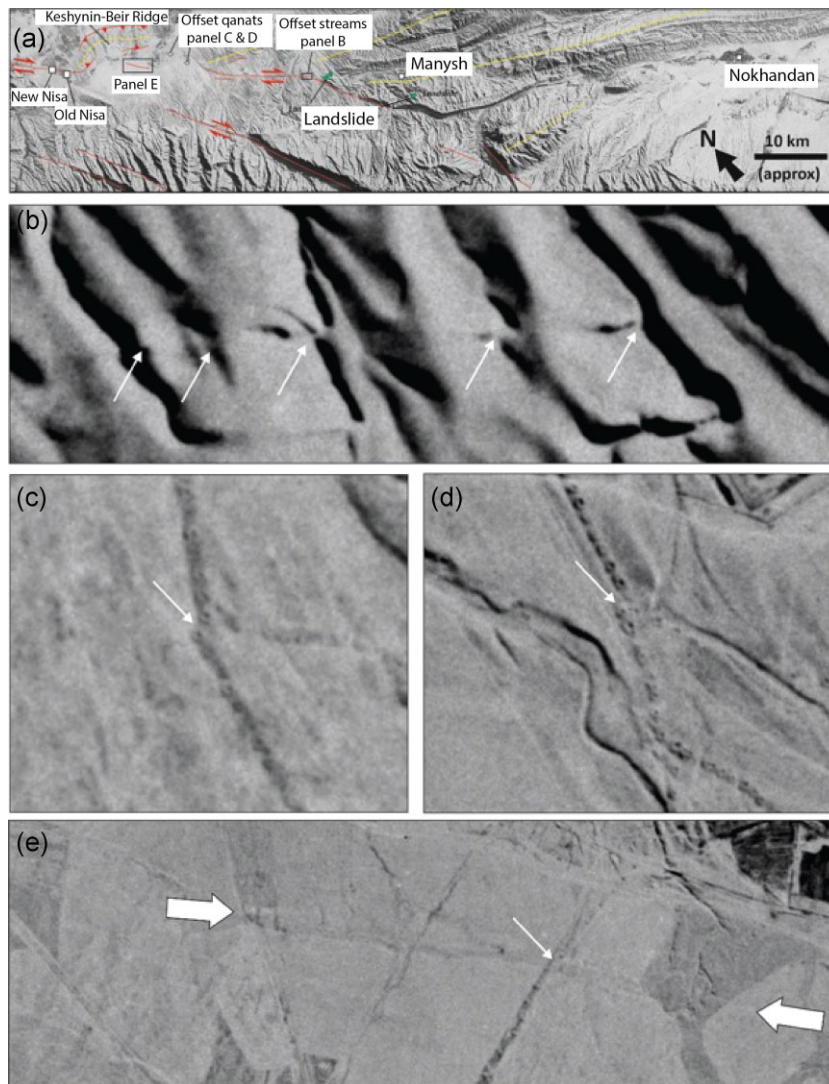


Figure 8. (a) Heritage Corona imagery from 1967 showing the region from Nisa in the northwest, to Nokhandan in the southeast (see Fig. 3 for location). Major fold axes are shown in yellow, and active faults in red. Three landslides south and west of Manysh are marked in green. Areas shown in later panels are marked. (b) aligned right-lateral stream displacements marked by white arrows. (c and d) Apparent qanat offsets of ~ 5 m. (e) Possible fault scarp south of Aşgabat, running between thick white arrows, with a further potential qanat offset marked by a thin white arrow.

6.2 Southeast of Aşgabat

Some of the most extensive ruptures reported from the 1948 occurred southeast of Aşgabat, along the Kharvardaghskiy fault, referred to as rupture zone B (Fig. 3). In Fig. 8(a) we show a Corona satellite image from 1967, extending from Aşgabat in the northwest to Nokhandan, in Iran, in the southeast, with the Kharvardaghskiy fault extending through the central part of the image. We have mapped geomorphic fault traces onto this image (in red) and the axes of major folds in bedrock (in yellow).

The Corona imagery was acquired 18 yr after the earthquake and is more likely to retain evidence of ground deformation from the 1948 earthquake, and potentially also from older events, than modern imagery. Near Manysh, we identify three ‘fresh’ landslide scars visible in proximity to the fault trace (Fig. 8a). We also identify a sharp NW–SE trace within alluvial surfaces, accompanied by consistent small stream displacements of ~ 15 m, as identified by shadowing, and marked by white arrows in Fig. 8(b). It is possible, though not confirmed, that this surface trace in the Corona image

represents surface rupturing from the 1948 earthquake. It is no longer visible in modern imagery due to urban development.

There is evidence for cumulative late quaternary displacement along the Kharvardaghskiy fault in the form of scarps in alluvial terraces, and the right-lateral displacement of streams and rivers. In Fig. 9(a) we show a Pleiades-derived DEM of the fault zone crossing heavily incised alluvial fan deposits immediately southeast of Aşgabat, at the very northern end of the mapped Rupture Zone B (Fig. 3). Georeferenced rupture locations from Rogozhin (1994) are shown as yellow lines (note that the locations are not necessarily accurate). In red, we highlight minor drainage channels within the alluvial fan that appear to be displaced right-laterally by ~ 40 m across two closely spaced fault traces, near the yellow lines. The northern of these two faults has a vertical component, with the northern side uplifted relative to the southern side. A third fault trace, again with a greater total uplift of the northern side, is visible near the top of Fig. 9(a). We could not find evidence of rupture from the 1948 earth along the third fault.

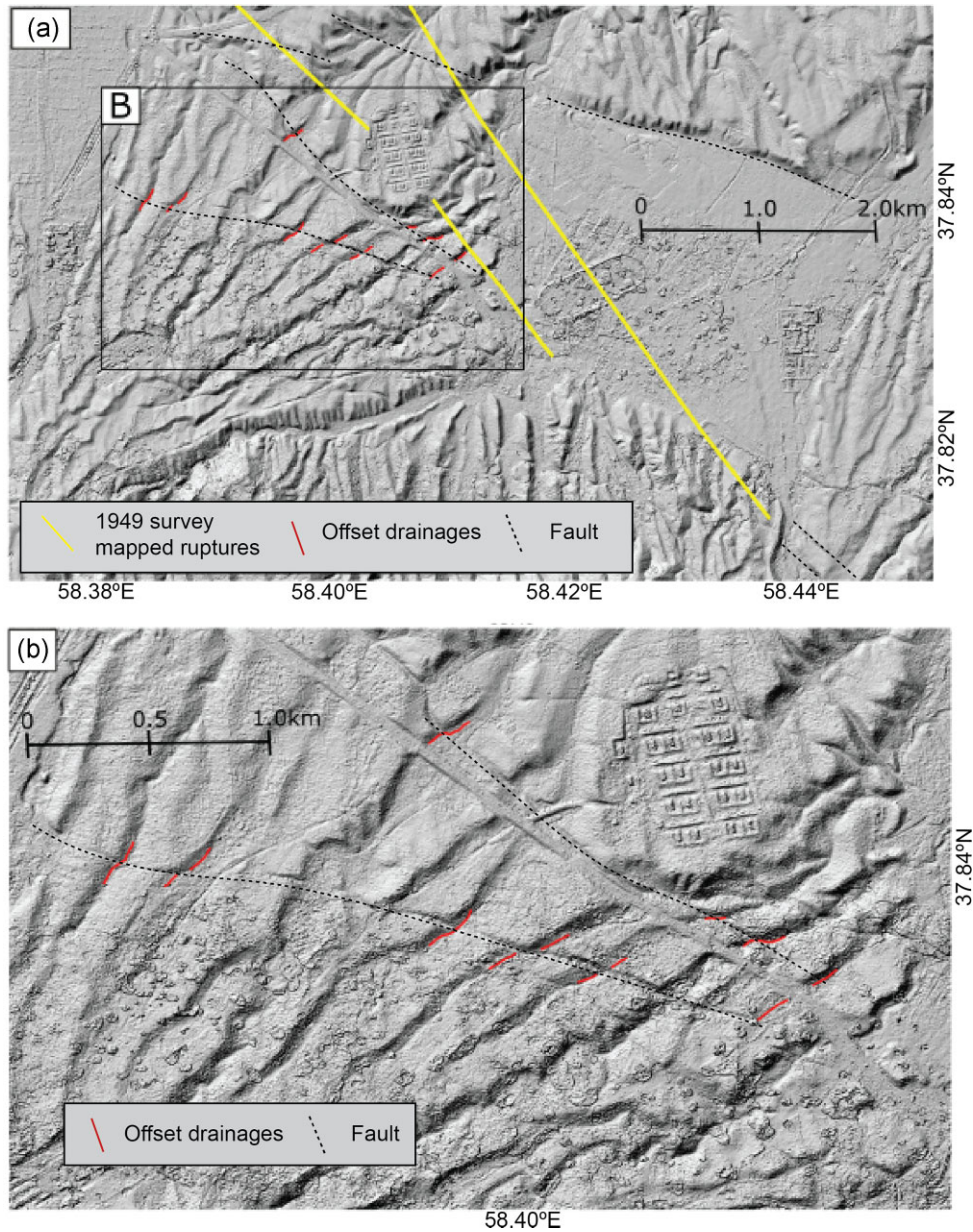


Figure 9. (a) Pléiades-derived DEM showing post-earthquake mapped ruptures southeast of Ashgabat [yellow lines (Rogozhin 1995)] adjacent to two scarps with cumulative right-lateral displacement of minor drainage channels within an incised alluvial fan surface, which we infer to be the scarps that ruptured in the earthquake. Towards the top of the image, a third fault scarp with clear up to the north displacement is visible, but does not appear to have ruptured at the surface in 1948. (b) Close-up of the two fault scarps with cumulative right-lateral stream displacements marked.

6.3 Ashgabat

Ashgabat city lies on an ~5-km-wide low-relief plain, occupying the area between the low hills of the Gyaursdag anticline to the south-east, and the Kesheny-Bair ridge to the northwest. The Kesheny-Bair ridge is a narrow (3 km wide) asymmetric anticline, with a maximum relief of ~70 m above the surrounding plains. It has a slight northward vergence, though with localized steepening on its southern side towards both east and western fold tips. Tilted basin sediments are exposed within drainage incised into the fold. The basin sediments are overlain by alluvial gravels that are parallel to the fold shape. Discontinuous ground deformations were observed within the ridge after the 1948 earthquake (e.g. Fig. 3).

No surface ruptures were reported in the region between the Kesheny-Bair ridge and the Gyaursdag hills, in the region closest

to Ashgabat itself. In Figs 8(c) and (d) we show apparent right-lateral offsets of two qanats (underground canals, identified from the aligned access shafts and spoil heaps), which are in a direct alignment between the southeastern margin of the Kesheny-Bair ridge and the right-lateral faults we identify in Fig. 9(a), which are part of Rupture zone B. In both cases the qanats are offset by an amount equal to the width of the spoil heaps, which is approximately 5 m, thought to be Sassanian or younger, >200 CE. A second possible fault scarp is identified south of the Kesheny-Bair ridge (Fig. 8e), along which there is a third possible qanat displacement.

To further investigate the potential for faulting extending through the southern districts of Ashgabat, and connecting Rupture zone B to the Kesheny-Bair ridge, we extract a number of topographic profiles through Pléiades-derived digital topography (Fig. 10). Each

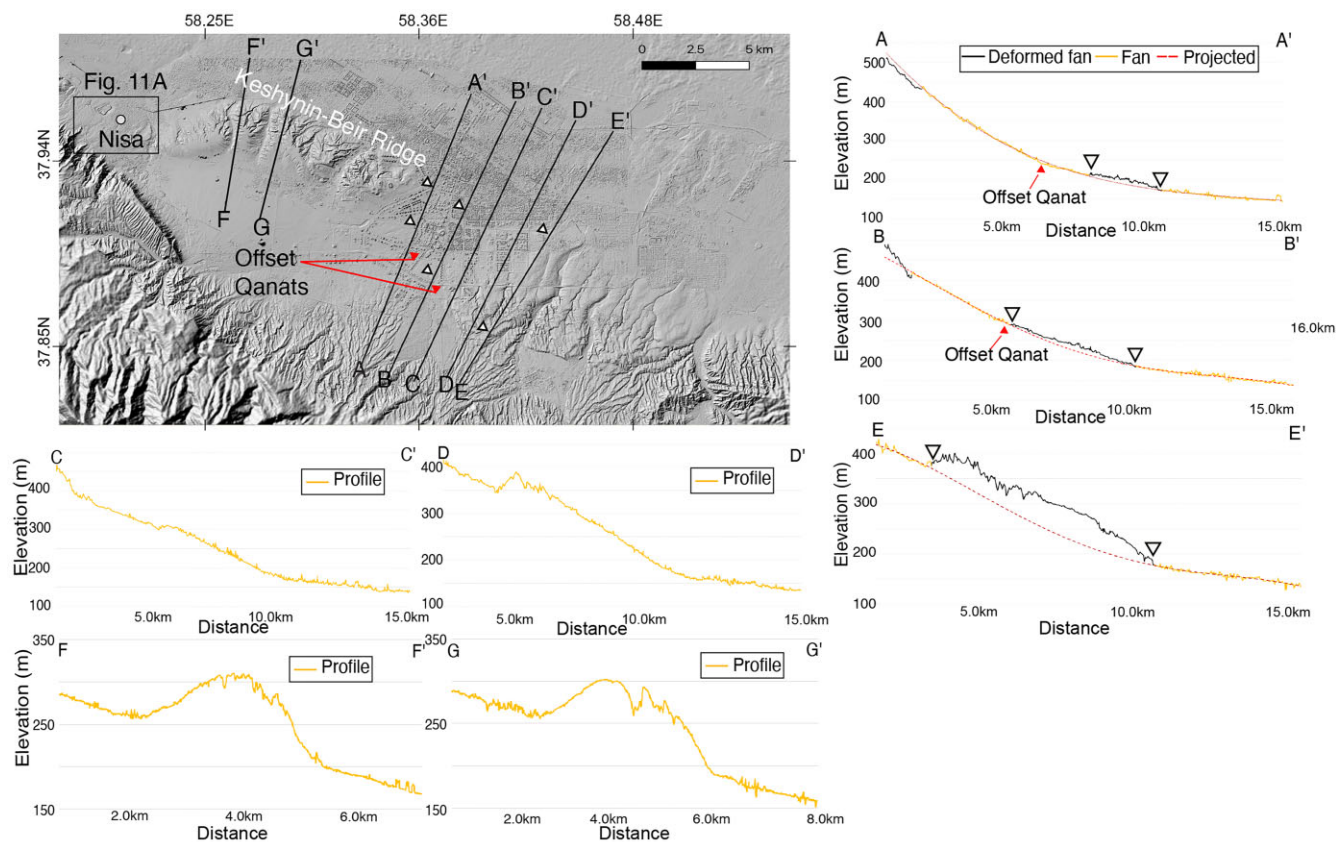


Figure 10. (a) Worldview-3 DEM of the Ashgabat area. White triangles show limits of folding as identified from topographic profiles. The red triangles show offset qanats (*cf.* Figs 8c and d).

of the profiles shows slight warping and folding of the alluvial surface, with the width and amplitude of the fold increasing to the southeast, and with a general change from northward vergence in the northwest to southward vergence in the southeast. In Fig. 10(a) we mark the margins of the topographic folding as white arrows, and mark the positions of the two offset qanats. There is close alignment in the positions of the offset qanat and the fold margin in profile B, whereas in profile A the offset qanat lies around 2 km south of the visible folding.

6.4 West of Ashgabat

West of Ashgabat an active fault extends northwest from the Keshynin-Bair ridge, traverses a low relief area at Nisa, and localizes along the base of the Köpetdag mountains (Fig. 10a). This section of fault is the easternmost ‘Gökdepe’ segment of the Main Köpetdag fault (MKDF) as defined by Dodds *et al.* (2022a, b). There are a number of archaeological sites in the region, but by far the most famous are the twin settlement mounds of Nisa. Both of these mounds show traces of early occupation in the Parthian era (*ca.* 247 BCE–224 CE), but are then subsequently reoccupied (Masson 1949; Viaz'mitina 1951; Invernizzi 1997), with substantial settlement in and around the northernmost mound (Fig. 10a). The fault trace passes immediately north of ‘Old’ Nisa, and cuts through the centre of ‘New’ Nisa (Fig. 11a).

The consistently northeast-facing fault scarp at New Nisa has a height of ~ 5 m. The northwestern wall of the walled city shows a sharp deflection at the scarp, consistent with ~ 20 m of right-lateral displacement (Fig. 11). This misalignment was seemingly

first identified by Poletaev (1986) through an examination of aerial photography and in the field. From current satellite imagery, the southeastern wall of the city does not show a clear displacement at the fault trace. If this apparent displacement of the northwest wall of the city is real, it suggests that the eastern wall of the fortress was rebuilt and realigned.

West of Nisa the fault runs along the base of the Köpetdag. Uplift of the southern side is apparent from suites of fluvial-alluvial terraces truncated at the fault. In Fig. 12, we show a suite of five terraces (labelled Q1 to Q5) preserved on the southern side of the Chuli river catchment. Here the terrace treads are extensive and well-preserved (Figs 12a and b), though modified by the presence of ancient sites of unknown age (particularly on the Q4 surface). The youngest surface (Q1) has no visible scarp at the fault. Topographic profiles through Q3, Q4 and Q5 show minimum vertical displacement of 10.4 ± 0.3 m, 24.1 ± 0.4 m and 59.1 ± 0.5 m. It is likely that these vertical displacements are accompanied by significant amounts of right-lateral slip. Roughly 5 km further west along the range front the fault cuts slightly into the rangefront, forming shutter ridges with ~ 150 m of displacement (Fig. 13), though there are no markers of lateral displacement at this site from which we can determine a strike-slip rate.

In order to determine the long-term dip-slip rate across the MKDF in this segment we collected three samples for IRSL dating, from a soil pit dug into the Q5 surface. The IRSL samples returned ages of 3.61 ± 0.88 k (100 cm), 98.8 ± 11 k (55 cm) and 102.7 ± 11 k (100 cm) (Table 4), which we note are similar in age to the prominent alluvial fan surfaces dated at 100 ± 5 ka by Walker *et al.* (2021), from 150 km further northwest along the range front. The sample

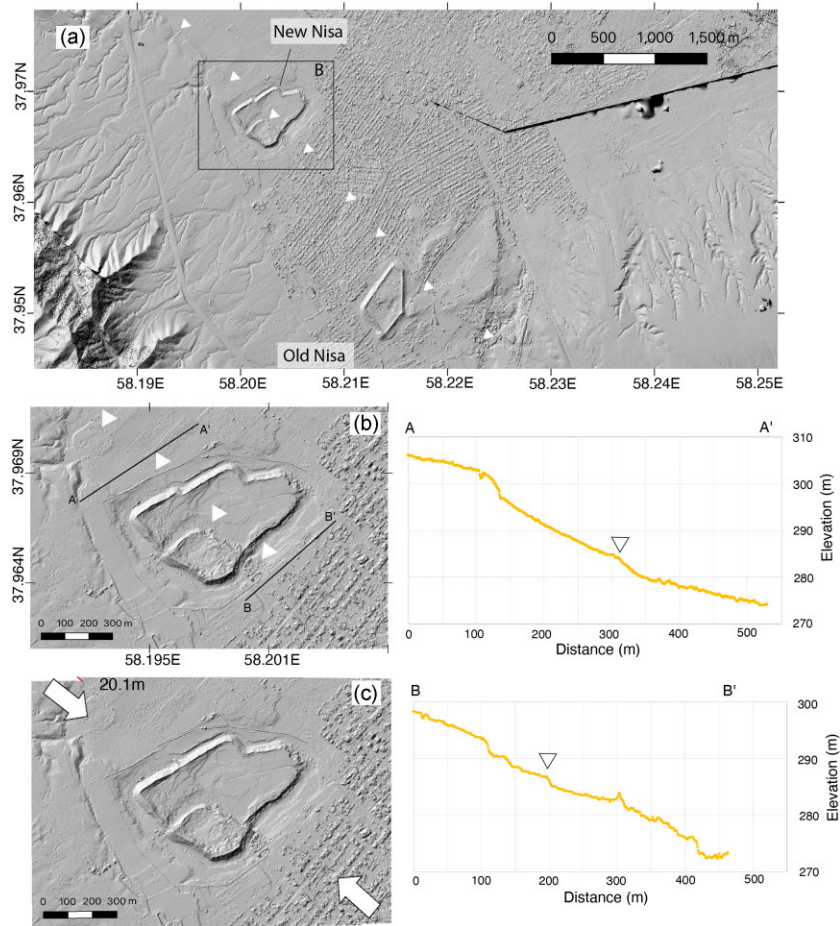


Figure 11. (a) DEM derived from Worldview-3 stereo imagery of the ancient city of Nisa. Triangles delineate the fault trace of the right-lateral MKDF. Box shown in (b). (b) Shows the zoomed DEM of the archaeological site New Nisa. The west wall shows an apparent offset at the fault trace. Profiles A–A' and B–B' show a scarp at the fault trace (at triangles). (c) Clipped (b) along the fault trace. Restoring the west wall of New Nisa measures at 20 m.

TK19-09 returning an age of 3.61 ± 0.88 k was produced by 4 grains. The surface shows evidence for human activity and is a possible source for contamination causing the outlying age, but this does not appear to have affected the loess layer above. The ~ 100 ka age of Q5, combined with a vertical offset of ~ 60 m allows us to estimate a minimum uplift rate of ~ 0.6 mm yr $^{-1}$. This rate assumes no erosion or deposition since the formation of QA and the vertical rate will be accompanied by an unknown, dominant, right-lateral strike-slip component.

7 DISCUSSION

By combining the focal mechanism and epicentral results (as summarized on Fig. 3) from this study with the isoseismal maps and the mapped ruptures from the 1949 survey (also on Fig. 3) we suggest that the earthquake nucleated immediately north of the city, and is likely to have ruptured several fault segments. The first causative fault (rupture zone B) extends southeast from Aşgabat for a distance of ~ 40 km, following a prominent right-lateral fault. Cumulative right-lateral displacements are visible as this fault crosses alluvial fan surfaces, and potential single-event scarps and associated landslides are identified in legacy Corona imagery from 1967.

Fracturing along the northern margin of the Gyaursdag anticline (Rupture zone A) likely indicates rupture of a southward-dipping

thrust fault, which may connect with Rupture zone B at depth. Although some of the ruptures along the Gyaursdag anticline may relate to secondary shaking effects, the en-echelon arrangement of fractures, the telescoping of water pipes, and the reported subsidence in the footwall of the fault from railroad levelling surveys, all suggest fault slip along the Gyaursdag structure. It is unlikely that the primary slip on the Gyaursdag fault reached the surface, with observed faulting relating to secondary fold growth structures.

Another potential rupture zone extends ~ 30 km northwest from the epicentre. Surface rupturing of 'Zone C' is associated with this fault segment. Although the rupturing itself is ambiguous in origin, and may be caused by liquefaction and other secondary effects, the post-1948 Railroad levelling survey indicates a mixture of uplift [33 cm at Büzmeýin (Bezmeim/Abadan)] west of Aşgabat and right lateral displacement (178–190 cm at Aşgabat), both of which are sited north of the observed surface ruptures and fault scarps that we have described. This proposed third segment does not have any visible expression at the surface, suggesting that additional active faults may exist north of the main range front of the Köpetdag, as also suggested by strain accumulation ~ 10 – 30 km north of the range front, measured further northwest using InSAR (Dodds *et al.* 2022b).

The overall rupture length is thus ~ 70 km, though with a gap in between the two main rupture zones of 10 km, giving a total of 80 km if this gap in surface observations is also included. The only

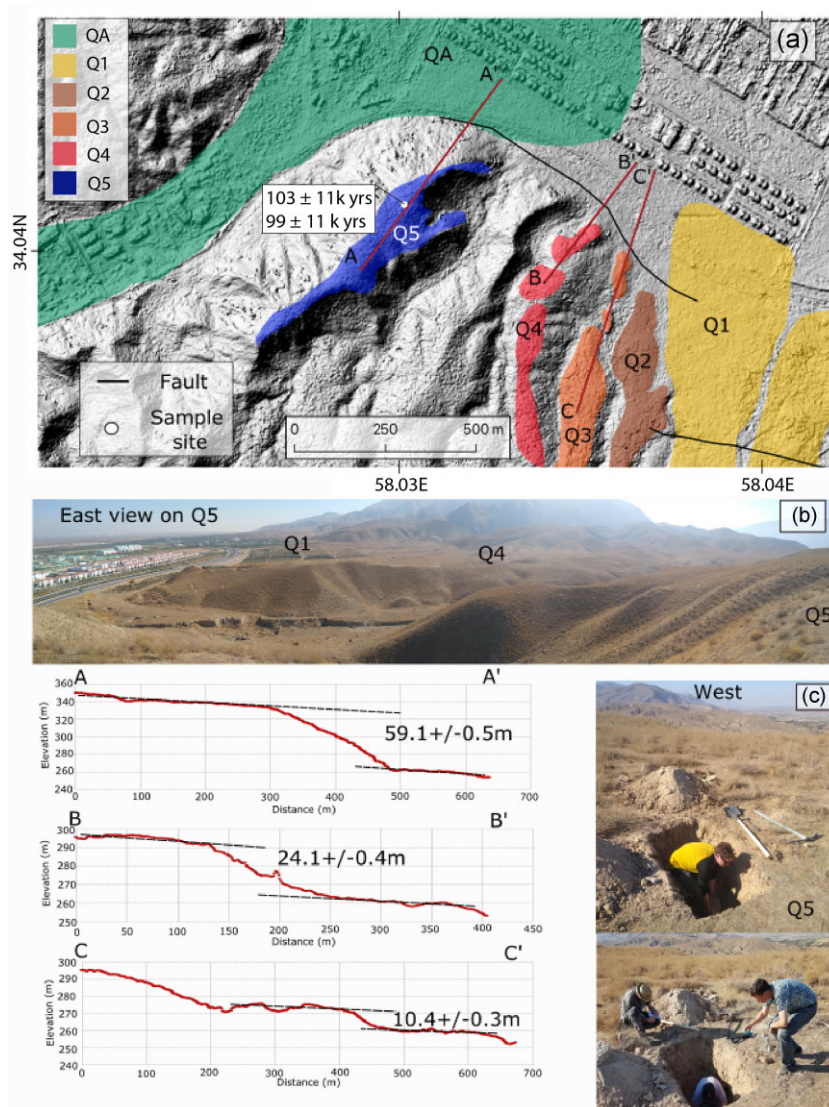


Figure 12. Pléiades DEM and geomorphic map of the region just to west of Ashgabat. Profiles show elevation taken from the DEM. The oldest geomorphic surface was sampled and IRSL ages calculated. Q5 is dated at $99\text{--}103 \pm 11$ kyr (see text). Photographs in B and C are taken looking East and West, respectively, at the sample site (white dot) on the Q5 surface shown in A.

measurement of coseismic lateral displacement is 178–190 cm of the railroad at Ashgabat, near the centre of the inferred rupture.

Using Wesnousky (2008) scaling relationships we estimate the M_w and slip from the total rupture length. From the observed total rupture length of 80 km we use the relationship

$$M_w = 5.56 + 0.87 \times \log(\text{length (km)}) \quad (3)$$

for strike-slip faulting, giving $M_w = 7.2$. To calculate the maximum slip, we use the log-linear relationship:

$$\text{slip (m)} = -5.02 + 5.02 \times \log(\text{length (km)}) = 4.5 \text{ m.} \quad (4)$$

These values are reasonable estimates given the previous calculations of moment magnitude of 7.3 (McKenzie 1972; Shebalin & Tatevossian 1996) and our estimate of $M_w = 7.29 \pm 1.4$.

Given the only measurement of lateral displacement is between 1.8 and 1.9 m in rupture zone, there is still uncertainty associated with the maximum and minimum slip.

The faults that are not known to have ruptured in the 1948 earthquake are also of interest. We have identified a continuation of faulting and folding northwest of rupture zone B that extends through southern districts of the modern city to connect with the Keshynin Bair ridge. This fault zone crosses open ground outside the 1948 urban extent, and we expect that any surface ruptures upon it would have been identified in the post-earthquake surveys. We therefore consider the gap in surface rupturing to be real. Two qanat lines are displaced right-laterally across the fault trace by ~ 5 m, close to the maximum slip calculated in for the 1948 Ashgabat earthquake. However, surface ruptures were not reported at this site suggesting that this offset occurred in unknown prior events.

The Keshynin Bair ridge is a northward-verging anticline (e.g. Fig. 10), which we infer to overlie a south-dipping thrust that joins at depth with the strike-slip fault on its southern side. A number of surface cracks were observed along the apex of the Keshynin Bair ridge, which may represent co-seismic fold growth, or may represent secondary effects. Northwest of the ridge, the right-lateral strike-slip fault trace is clearly visible in satellite imagery, and appears

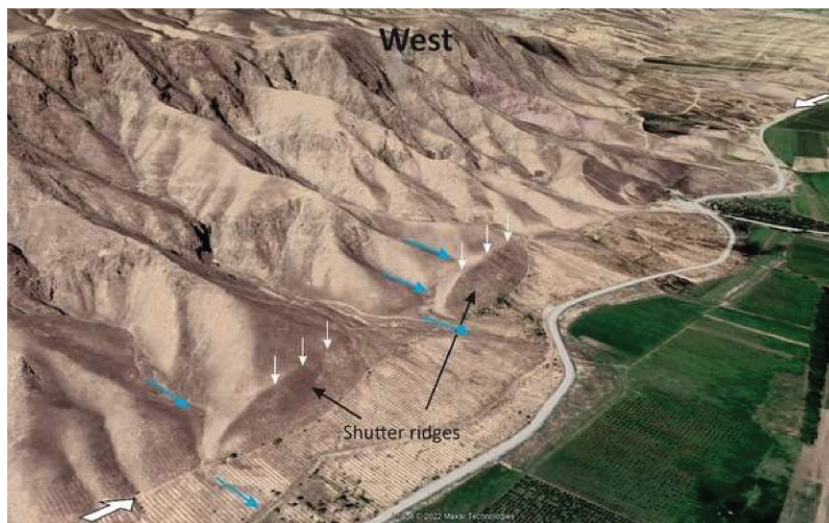


Figure 13. Perspective view looking west across the Main Köpetdag fault, running between the thick white arrows, ~5 km northwest from the region shown in Fig. 12(a) (centre coordinate at 38.072590°N, 57.975358°E, see Fig. 3 for location). The fault trace cuts across hillslopes (scarps shown by vertical white arrows) and has right-laterally displaced the lower portions of the hillslopes, which now form shutter ridges. Drainage channels (blue) are displaced by ~150 m around the ends of these shutter ridges.

to offset the outer walls of New Nisa, whose fortified walls are believed to be laid out initially in the Parthian era (third to second century CE). Again, there is no record at this site of rupturing caused by the 1948 earthquake, and the archaeologists who were working at the site were most active during this period (some of the archaeologists on the team were sadly even injured or killed in the event; Masson 1949; Viaz'mitina 1951). The displacements of ~20 m, if real therefore, indicate several prior events have occurred since the walls were constructed.

Poletaev (1986) identified a 1.5 m difference in height between the northeastern and southwestern sectors of the walled city, bisected by the fault. He further subdivided the southwestern sector into two distinct zones, the northwestern being slightly higher than the southern, although the latter apparently had better preservation of archaeology. This interpretation seems to be at odds, however, with the archaeological data from the site gathered by the South-Turkmenistan Archaeological Comprehensive Expedition (IUTAKE) in the 1940s, which identified the southern area as the higher mound of an inner walled citadel (Masson 1949). It is tricky, then, to disambiguate the synthetic structural components of the city, its walls and landscaping, from the perceived deformation of the land. Furthermore, it was observed already in the 1940s that local farmers were modifying and reutilizing areas of the walled city and citadel (Pugachenkova 1949).

The history of the settlement and its walls might have been disambiguated through the stratigraphy of the test-trenches and sections dug around the city, but the majority proved inconclusive in terms of determining major topographical shifts. Based on the work of the IUTAKE 1940s missions, they observed that the site was probably occupied, and indeed walled initially between the third and second centuries BCE, with general signs of decline going into the first millennium CE (Masson 1949; Viaz'mitina 1951). According to the same authors, there is resumed activity in the 4th–8th centuries CE and then again between the 11th–13th and 15th–17th centuries, based on ceramic chronology.

It is possible to suggest that the periodic abandonment of the site might be linked to seismic activity. Based on the identification of a sudden collapse in the excavations at the nearby site of Old

Nisa, Masson and colleagues proposed a date in the first century BCE or CE for a significant earthquake, which has subsequently been quoted as definitive in the major earthquake catalogues for the region (Pugachenkova 1949). An additional fifth century event was similarly identified by archaeologists at Old Nisa from collapse evidence but was later refuted and indeed is not mentioned in the interpretation of the sequence at New Nisa (Davidovich 1951).

Turning to the 8th–10th century hiatus at New Nisa, the explanation for abandonment is unclear. It is particularly pertinent to note that evidence of significant decline includes the ruin of the city walls and their complete lack of upkeep, to the extent that domestic buildings were being built on top of the collapsed defences (Viaz'mitina 1951). As Pilipko points out, the interpretation for the stratigraphy for this period is difficult to unravel at the site, with complex reuse, and his attempts to revisit this sequence have not been able to define the abandonment more clearly (Pilipko 2010). Meanwhile 10th century historical sources on the city seem to indicate that it was flourishing, although it is unclear exactly the material on which this account is based, or indeed the specific zones of the city which are being described (al-Muqaddasi 2001). Considering this difficulty of interpretation, alongside the significant general reappraisal of medieval ceramic chronologies since the excavations took place, it might be possible to connect the later abandonment to the known catastrophic seismic event of 943 CE, recorded by 12th century historian Ibn al-Athir and others. Based on additional evidence for landslides around the same time elsewhere, Ambraseys & Melville (1982) place the event instead in the southern part of the Köpetdag. Until further archaeological and palaeoseismic work can refine the location and impacts of the 943 earthquake, it is possible that the traces of displacement being observed relate to this period, after which the walls are known to be rebuilt.

Finally, the improved determination of the 1948 earthquake source, and mapping of faults around the wider Ashgabat region, is useful in refining our understanding of the regional fault kinematics. We have shown that Ashgabat is sited at a transition from right-lateral faulting cutting through the interior of the Köpetdag mountains as part of the BQFZ (Fig. 1), to faults that run along the range front as the easternmost parts of the MKDF. As such, the faults here are

likely to be contributing to the NNW motion of the South Caspian Basin relative to Eurasia. Further northwest, the MKDF has consistent long-term geological $9.1 \pm 1.3 \text{ mm yr}^{-1}$ (Walker *et al.* 2021), and decadal $9 \pm 2 \text{ mm yr}^{-1}$ (Dodds *et al.* 2022a) slip rates. From existing GNSS measurements (e.g. Mousavi *et al.* 2013; Khorrami *et al.* 2019) and kinematic models (e.g. Hollingsworth *et al.* 2010; Walker *et al.* 2021) we expect those rates to decrease eastwards, as the South Caspian motion is accommodated at its eastern end by block rotations and fault slip in the BQFZ. The apparent right-lateral displacements of cultural sites around Aşgabat are interesting in this respect, as they suggest relatively rapid accumulation of slip ($\sim 8\text{--}9 \text{ mm yr}^{-1}$) over the last few thousand years in an area that we would expect the faults to have relatively low overall slip-rates. Either the displacements are misleading, the fault slip-rates are higher than we expect or, potentially, we are seeing the effects of millennial scale variability in fault slip. Detailed palaeoseismic investigation and slip-rate determination are required to test which of these is correct.

8 CONCLUSION

We show that the 1948 Aşgabat earthquake was a right-lateral strike-slip event most likely nucleating immediately north of Aşgabat, and involving bilateral rupture on at least two separate faults with a total length of $\sim 80 \text{ km}$. Active faults within the southern districts of Aşgabat and adjacent areas to the west do not appear to have ruptured at the surface in the 1948 earthquake, and yet show apparent significant displacement in cultural sites, including qanats (Sassanian or younger, $>200 \text{ CE}$), and the walls of Nisa (Parthian, $\sim 200 \text{ BCE}$). These observations suggest continuing local earthquake hazard in Aşgabat. The faults involved in the 1948 earthquake are at the easternmost end of the Köpetdag strike-slip fault system and show a transition of slip from the range-front right-lateral faults to those that cut through the Köpetdag interior, as part of the BQFZ. The northwestern fault segment is not apparent in the geomorphology and is sited $\sim 15 \text{ km}$ north of the prominent range-front, highlighting the potential hazards posed by ‘concealed’ active faults in low-relief regions.

ACKNOWLEDGMENTS

This work was supported by the Leverhulme Trust Research Project Grants ‘EROICA’ (RPG-2018–371) and ‘NEPTUNE’ (RPG-2018–243), by the NERC-ESRC Increasing Resilience to Natural Hazards program ‘Earthquakes without Frontiers’ (NE/J02001X/1), the NERC-funded COMET (GA/13/M/031) and allocation 0009090 from the Research England GCRF Support Fund. Pléiades satellite imagery was obtained through the Committee for Earth Observing Satellites (CEOS) Seismic Hazard demonstrator. Worldview-3 satellite imagery was obtained through the NERC grant ‘Looking into the Continents from Space’ (NE/K011006/1). We would like to thank the reviewers and editor of this study for their feedback and comments.

DATA AVAILABILITY

Pléiades derived Digital Elevation Models used in this study are available in point cloud form on the OpenTopography website <https://opentopography.org/>. Digitized seismograms are available on EarthScope (IRIS and UNAVCO) <https://www.earthscope.org/>.

REFERENCES

- AgiSoft PhotoScan Professional (Version 2.0) Software (2021). Retrieved from <https://www.agisoft.com/downloads/installer/>.
- al-Muqaddasi, 2001. The best divisions for knowledge of the regions: ahsan al-Taqāsīm Fī Marifat al-Aqālim. Translated by Basil Collins. Reading: Garnet.
- Ambraseys, N.N. & Melville, C.P., 1982. *A History of Persian Earthquakes*. Cambridge University Press. ISBN 0 521 24112 X.
- Ambraseys, N.N., 1997. The Krasnovodsk (Turkmenistan) earthquake of 8 July 1895. *J. Earthq. Eng.*, **1**(02), 293–317.
- Antoine, S.L., Klinger, Y., Delorme, A., Wang, K., Bürgmann, R. & Gold, R.D., 2021. Diffuse deformation and surface faulting distribution from submetric image correlation along the 2019 Ridgecrest, California, ruptures. *Bull. seism. Soc. Am.*, **111**(5), 2275–2302.
- Barbot, S., Luo, H., Wang, T., Hamiel, Y., Piatibratova, O., Javed, M.T., Braitenberg, C. & Gurbuz, G., 2023. Slip distribution of the February 6, 2023 m_w 7.8 and M_w 7.6, Kahramanmaraş, Turkey earthquake sequence in the East Anatolian Fault Zone. *Seismica*, **2**(3), doi:10.26443/seismica.v2i3.502.
- Berberian, M. & Yeats, R.S., 2001. Contribution of archaeological data to studies of earthquake history in the Iranian Plateau. *J. Struct. Geol.*, **23**(2–3), 563–584.
- Bergman, E., Benz, H., Yeck, W., Karasözen, E., Engdahl, E.R., Ghods, A., Hayes, G. & Earle, P., 2022. A global catalog of calibrated earthquake locations. *Seismol. Res. Lett.*, **94**(1), 485–495.
- Bormann, P. & Saul, J., 2008. The new IASPEI standard broadband magnitude $m(B)$. *Seismol. Res. Lett.*, **79**, 698–705.
- Bormann, P., 2012. New Manual of Seismological Observatory Practice (NMSOP-2), IASPEI, GFZ German Research Centre for Geosciences, Potsdam; 10.2312/GFZ.NMSOP-2urn:nbn:de:kobv:b103-NMSOP-2. <http://nmsop.gfz-potsdam.de>. doi: 10.2312/GFZ.NMSOP-2urn:nbn:de:kobv:b103-NMSOP-2.
- Butovskaya, E.M. & Kovalenko, Y.A.G., 1955. Osobennosti karty isoseist Ashkhabadskovo zemletryaseniya 5–6 Oktyabrya 1948 goda i deformaziya zemnoi poverkhnosti v rayone Ashkhabada po dannym nivelirovok 1942–1952 gg. in *Meteorologiya i gidrologiya v Uzbekistane*, Izd. Akad. Nauk Uzb. S.S.R.
- Charlier, C.H. & Van Gils, J.M., 1953. *Liste des Stations Seismologiques Mondiales. L'Association Internationale de Seismologie*, Observatoire Royal de Belgique a Uccle Service Seismologique.
- Cooke, M.L. & Pollard, D.D., 1997. Bedding-plane slip in initial stages of fault-related folding. *J. Struct. Geol.*, **19**(3–4), 567–581.
- Copley, A. & Jackson, J., 2006. Active tectonics of the Turkish-Iranian Plateau. *Tectonics*, **25**(6), doi:10.1029/2005TC001906.
- Davidovich, A., 1951. Report on the 1947 excavations in the area of the Square Hall of Old Nisa, Ashgabat, in *Proceedings of the South Turkmenistan Archaeological Complex Expedition*, pp. 108–142.
- Djamour, Y. *et al.* 2010. GPS and gravity constraints on continental deformation in the Alborz mountain range, Iran. *Geophys. J. Int.*, **183**(3), 1287–1301.
- Dodds, N., Begejev, G., Bezmenov, Y., Gruetznern, C., Mirzin, R., Rhodes, E., Walker, R.T. & Wordsworth, P., 2022a. A major medieval earthquake on the main Köpetdag (Kopet Dag) Fault, Turkmenistan. *Bull. seism. Soc. Am.*, **112**(4), 2189–2215.
- Dodds, N., Daout, S., Walker, R.T., Begejev, G., Bezmenov, Y., Mirzin, R. & Parsons, B., 2022b. Interseismic deformation and strain-partitioning along the Main Köpetdag Fault, Turkmenistan, with Sentinel-1 InSAR time-series. *Geophys. J. Int.*, **230**(3), 1612–1629.
- Engdahl, E.R., van der Hilst, R. & Buland, R., 1998. Global teleseismic earthquake relocation with improved travel times and procedures for depth determination. *Bull. seism. Soc. Am.*, **88**(3), 722–743.
- England, P. & Jackson, J., 2011. Uncharted seismic risk. *Nat. Geosci.*, **4**(6), 348–349.
- Fedorov, P.V., 1998. Ashgabat-1948. Recollection of an eyewitness. *Vestn. Otd. Geol. Geofiz. Geokhim. Gorn. Nauk Ross. Akad. Nauk*, **2**, 20–25.

- Golinskiy, G.L. & Nepesov, R.D., 1968. Seismicity characteristics of Turkmenistan and adjacent Iran regions on the macroseismic materials. in *Seysmichnost, Turkmeniyi*, pp. 51–151, Ashgabat Turkmenistan.
- Gorshkov, G.P., 1984. *Seismotectonics of the Kopet Dagh*, 272 pp., Nauka.
- Gorshkov, G.P., Geological settings of the Ashgabat earthquake occurrence (a section from the Report on Works of the Commission of the USSR Academy of Sciences in 1948), Vestn. Otd. Geol. Geofiz. Geokhim. Gorn. Nauk Ross. Akad. Nauk, 1998, no. 2, pp. 57–62.
- Grützner, C. *et al.* 2017a. Assessing the activity of faults in continental interiors: palaeoseismic insights from SE Kazakhstan. *Earth planet. Sci. Lett.*, **459**, 93–104.
- Grützner, C., Walker, R.T., Abdrakhmatov, K.E., Mukambayev, A., Elliott, A.J. & Elliott, J.R. (2017b). Active tectonics around Almaty and along the Zailisky Alatau Range front. *Tectonics*, **36**, 2192–2226.
- Gutenberg, B. & Richter, C. F. 1956 Earthquake magnitude, intensity, energy, and acceleration: (Second paper). *Bulletin of the Seismological Society of America* **46** 2 105–145
- Hayes, G.P., Bergman, E., Johnson, K.L., Benz, H.M., Brown, L. & Meltzer, A.S., 2013. Seismotectonic framework of the 2010 February 27 MW 8.8 Maule, Chile earthquake sequence. *Geophys. J. Int.*, **195**(2), 1034–1051.
- Heimann, S. *et al.* 2017. Pyrocko—an open-source seismology toolbox and library.
- Hollingsworth, J., Fattahi, M., Walker, R., Talebian, M., Bahroudi, A., Bolourchi, M.J., Jackson, J. & Copley, A., 2010. Oroclinal bending, distributed thrust and strike-slip faulting, and the accommodation of Arabia–Eurasia convergence in NE Iran since the Oligocene. *Geophys. J. Int.*, **181**(3), 1214–1246.
- Hollingsworth, J., Jackson, J., Walker, R. & Nazari, H., 2008. Extrusion tectonics and subduction in the eastern South Caspian region since 10 Ma. *Geology*, **36**(10), 763–766.
- Hollingsworth, J., Jackson, J., Walker, R., Reza Gheitanchi, M. & Javad Bolourchi, M., 2006. Strike-slip faulting, rotation, and along-strike elongation in the Kopeh Dagh mountains, NE Iran. *Geophys. J. Int.*, **166**(3), 1161–1177.
- International Seismological Centre, 2022. On-line Bulletin. <https://doi.org/10.31905/D808B830>.
- Invernizzi, A. (1997). Parthian Nisa: new lines of research. *Iran Caucasus*, **1**, 107–119. <http://www.jstor.org/stable/4030744>
- Jackson, J. & McKenzie, D. 1984. Active tectonics of the Alpine—Himalayan Belt between western Turkey and Pakistan. *Geophys. J. Int.*, **77**(1), 185–265.
- Jackson, J., Priestley, K., Allen, M. & Berberian, M., 2002. Active tectonics of the south Caspian basin. *Geophys. J. Int.*, **148**(2), 214–245.
- Jordan, T.H. & Sverdrup, K.A., 1981. Teleseismic location techniques and their application to earthquake clusters in the South-Central Pacific. *Bull. seism. Soc. Am.*, **71**(4), 1105–1130.
- Karasözen, E., Nissen, E., Bergman, E.A. & Ghods, A., 2019. Seismotectonics of the Zagros (Iran) from orogen-wide, calibrated earthquake relocations. *J. geophys. Res.*, **124**(8), 9109–9129.
- Kennett, B.L.N., Engdahl, E.R. & Buland, R., 1995. Constraints on seismic velocities in the Earth from traveltimes. *Geophys. J. Int.*, **122**(1), 108–124.
- Khorrami, F. *et al.* 2019. An up-to-date crustal deformation map of Iran using integrated campaign-mode and permanent GPS velocities. *Geophys. J. Int.*, **217**(2), 832–843.
- Kolibacv, V.A. 1962. O smeshenii geodezicheskikh punktov v rayone Ashkhabadskovo zem lctryascnya 1948 g. Geode zia i Kartografiya 5, Geodezizdat.
- Kulikova, G. & Krüger, F., 2015. Source process of the 1911 M 8.0 Chon-Kemin earthquake: investigation results by analogue seismic records. *Geophys. J. Int.*, **201**(3), 1891–1911.
- Kulikova, G. & Krüger, F., 2017. Historical seismogram reproductions for the source parameters determination of the 1902, Atushi (Kashgar) earthquake. *J. Seismol.*, **21**(6), 1577–1597.
- Kulikova, G., Schurr, B., Krüger, F., Brzoska, E. & Heimann, S., 2016. Source parameters of the Sarez-Pamir earthquake of 1911 February 18. *Geophys. J. Int.*, **205**(2), 1086–1098.
- Kurushin, R.A., Bayasgalan, A., O’Lziybat, M., Enhtuvshin, B., Molnar, Peter, Bayarsayhan, Ch., Hudnut, K.W. & Lin, J., 1998. *GSA SPECIAL PAPERS: The Surface Rupture of the 1957 Gobi-Alay, Mongolia, Earthquake*, Vol. **320**, Geological Society of America.
- Laske, G., Masters, G., Ma, Z. & Pasyanos, M., 2013. Update on crust1.0—a 1-degree global model of Earth’s crust, in *EGU General Assembly 2013*, 7–12 April 2013, Vienna, Austria, id. EGU2013-2658.
- Liapin, A., 2006. The excavations of A. A. Marushchenko at Ak-Tepe. Problems of history, philology. *Culture*, **16**(1), 267–292.
- Mackey, K.G. & Bergman, E., 2014. Ground-truth locations for the Mangyshlak peaceful nuclear explosion sequence, western Kazakhstan. *Bull. seism. Soc. Am.*, **104**(4), 2116–2119.
- Masson, M.E., 1949. ‘Gorodishcha Nisy v Selenii Bagir i Ikh Izuchenie’, in *Trudy IUTAKE 1*, pp. 16–115, ed. Masson, M.E., Izdatel’stvo Turkmen-skogo Filiala Akademii Nauk SSSR.
- McKenzie, D., 1972. Active tectonics of the Mediterranean Region. *Geophys. J. Int.*, **30**(2), 109–185.
- Mousavi, Z., Walpersdorf, A., Walker, R.T., Tavakoli, F., Pathier, E., Nankali, H.R.E.A., Nilfouroushan, F. & Djamour, Y., 2013. Global Positioning System constraints on the active tectonics of NE Iran and the South Caspian region. *Earth planet. Sci. Lett.*, **377**, 287–298.
- NASA Shuttle Radar Topography Mission (SRTM), 2013. *Shuttle Radar Topography Mission (SRTM) Global*. Distributed by OpenTopography. Accessed: 2023-11-01.
- Nicol, A. & Nathan, S., 2001. Folding and the formation of bedding-parallel faults on the western limb of Grey Valley Syncline near Blackball, New Zealand. *N.Z. J. Geol. Geophys.*, **44**(1), 127–135.
- Nikonov, A.A., 1998. Aşgabat Earthquake: half a century later. *Bull. Russ. Acad. Sci.*, **68**(9), 789–797.
- Okal, E.A., 2015. Historical seismograms: preserving an endangered species. *GeoResJ*, **6**, 53–64.
- Orasymbetov, N.O., Serdyukov, M.M. & Shanin, S.A., 1960. The 1948 Ashgabat Earthquake (in Russian). Государственноеиздательство литературы по трюительству архитектуре истроительным материалам, Moscow.
- Ou, Q., Kulikova, G., Yu, J., Elliott, A., Parsons, B. & Walker, R., 2020. Magnitude of the 1920 Haiyuan earthquake reestimated using seismological and geomorphological methods. *J. geophys. Res.*, **125**(8), e2019JB019244.
- Pho, H.-T. & Behe, L., 1972. Extended distances and angles of incidence of P waves. *Bull. seism. Soc. Am.*, **62**(4), 885–902.
- Pilipko, V.N., 2007. Some results of the archaeological investigations at Old Nisa. *Rossiyskaya Arkheologiya*, **1**, 150–158.
- Pilipko, V.N., 2010. Stratigrafiya i Topografiya Gorodishcha Novaia Nisa, in *Drevnie Tsvivilizatsii Na Srednem Vostoke. Arkheologiya, Istoriya, Kul’tura*, ed. Bolelov, S.B., Gosudarstvennyy muzei Vostoka.
- Poletaev, A.I., 1986. *Seismotektonika Zony Glavnogo Kopetdagского Razloma*. Moscow: Nauka.
- Pugachenkova, G.A., 1949. ‘Rekonstruktsiia “Kvadratnogo Zala” Parfianskogo Ansambliya Staroi Nisy’, in *Trudy IUTAKE 1*, pp. 141–146, ed. Masson, M.E., Izdatel’stvo Turkmen-skogo Filiala AN SSSR.
- Pugh, D.J. & White, R.S., 2018. MTfit: a bayesian approach to moment tensor inversion. *Seismol. Res. Lett.*, **89**, 1507–1513.
- Pugh, D.J., White, R.S. & Christie, P.A.F., 2016. A Bayesian method for microseismic source inversion. *Geophys. J. Int.*, **206**(2), 1009–1038.
- QGIS Development Team, 2021. QGIS Geographic Information System. Open Source Geospatial Foundation Project. <https://qgis.org>.
- Rezanov, I.A., 1957. The Ashkhabad Earthquake of 1948 and its geological background, Academy of Science USSR.
- Rogozhin, E.A., 1995. Tectonic position and geologic manifestations of the Ashkhabad 1948 earthquake. *Izv. Phys. Solid Earth*, **30**(9), 747–758.
- Rogozhin, E.A., 2012. *Ocherki Regional’noi Seismotektoniki (Overviews of Regional Seismotectonics)*, Inst. Fiz. Zemli Ross. Akad. Nauk., ISBN 978-5-91682-017-1.
- Rustanovich, D.N. & Shirokova, E.I., 1964. Some results of a study of the Ashkhabad earthquake of 1948, *Izv. Akad. Nauk S.S.S.R. (ser. Geofiz.)*, **12**, 1077–1080. (Transl. by Am. Geoph. Union).

- Rustanovich, D.N., 1967. Seismicity of the Turkmen Territory and 1948 Ashkhabad earthquake. *Voprosy Inzhenernoy Seysmologiyi*, **12**, 95 pp., Nauka, Moscow.
- Schweitzer, J., 2001. HYPOSAT—an enhanced routine to locate seismic events. *Pure appl. Geophys.*, **158**(1), 277–289.
- Shabaniyan, E., Bellier, O., Siame, L., Arnaud, N., Abbassi, M.R. & Cochemé, J.J., 2009. New tectonic configuration in NE Iran: active strike-slip faulting between the Kopeh Dagh and Binalud mountains. *Tectonics*, **28**(5), doi:10.1029/2008TC002444.
- Shebalin, N.V. & Tatevossin, R.E., 1996. Catalogue of strong earthquakes ($M \geq 6.0$) for the Global Seismic Hazard Assessment Program test area 'CAUCASUS'. Historical and Prehistorical Earthquakes in the Caucasus.
- Shebalin, N.V., 1974. *Foci of Large Earthquakes at the USSR Territory*, 53pp., Nauka.
- Shirokova, E.I., 1967. *General Features in the Orientation of Principal Stresses in Earthquake Foci in the Mediterranean-Asia Seismic Belt*, USSR Academy of Sciences, Institute of Physics of the Earth, pp. 12–22
- Sidorin, A.Ya., 2019. Effects and lessons of the 1948 Ashgabat earthquake, *Seismic Instrum.*, **55**(3), 271–282.
- Sukacheva, M.P. & Kazanli, D.N., 1949. Report on the geologic studies of the October 6th 1948 Ashkhabad Earthquake. 123 pp., Ashkhabad.
- Tchalenko, J.S., 1975. Seismicity and structure of the Kopet Dagh (Iran, USSR), *Phil. Trans. R. Soc. Lond.*, **278**(1275), 1–28.
- Tsai, C.-H. et al., 2022. Probing the upper end of intracontinental earthquake magnitude: a prehistoric example from the Dzhungarian and Lepsy Faults of Kazakhstan, *Tectonics*, **41**, e2022TC007300, doi:10.1029/2022TC007300.
- Viaz'mitina, M.I. 1951. 'Arkheologicheskoe Izuchenie Gorodishcha Novaia Nisa v 1947 Godu', in *Trudy IUTAKE 2*, pp. 147–169, ed. Masson, M.E., Izdatel'stvo Turkmenskogo Filiala AN SSSR.
- Walker, R.T. et al. 2021. Slip-rate on the Main Köpetdag (Kopeh Dagh) strike-slip fault, Turkmenistan, and the active tectonics of the South Caspian. *Tectonics*, **40**(8), e2021TC006846.
- Walker, R.T., Bergman, E.A., Szeliga, W. & Fielding, E.J., 2011. Insights into the 1968–1997 dasht-e-bayaz and Zirkuh earthquake sequences, eastern Iran, from calibrated relocations, In-sar and high-resolution satellite imagery. *Geophys. J. Int.*, **187**(3), 1577–1603.
- Wesnousky, S., 2008. Displacement and geometrical characteristics of earthquake surface ruptures: issues and implications for seismic-hazard analysis and the process of earthquake rupture. *Bull. seism. Soc. Am.*, **98**, 1609–1632.
- Wimpenny, S. & Watson, S.C., 2020. gWFM: a global catalog of moderate-magnitude earthquakes studied using teleseismic body waves. *Seismol. Res. Lett.*, **92**(1), 212–226.
- Yeck, W.L., Weingarten, M., Benz, H.M., McNamara, D.E., Bergman, E.A., Herrmann, R.B. & Earle, P.S., 2016. Far-field pressurization likely caused one of the largest injection induced earthquakes by reactivating a large preexisting basement fault structure. *Geophys. Res. Lett.*, **43**(19), doi:10.1002/2016gl070861